Mineralium Deposita
https://doi.org/10.1007/s00126-024-01253-8

ARTICLE

Sulfur isotopes in Archaean crustal reservoirs constrain the transport and deposition mechanisms of nickel-sulfides in komatiites

Anne B. Virnes[1] · Marco L. Fiorentini[1] · Stefano Caruso[1,2] · Kim Baublys[3] · Quentin Masurel[1] · Nicolas Thebaud[1]

Received: 17 November 2023 / Accepted: 16 February 2024

Abstract

Assimilation and prolonged suspension of crust-derived sulfide liquid in komatiites are essential to form Ni-rich mineralisation. Evaluating the spatial relationship between komatiite-hosted Ni mineralisation and crustal S sources may thus provide insights into mechanisms of transport, metal enrichment and deposition of assimilated sulfide liquid. This study applied facies analysis and S isotopes to sulfides in Ni-mineralised komatiites and stratigraphically underlying bimodal volcanic-volcaniclastic and sedimentary rocks, which formed during rifting in the Agnew-Wiluna Greenstone Belt, Western Australia. The results revealed a lateral variation from rift-distal sedimentary sulfides, through sulfidic BIF, to rift-proximal VMS-style sulfides, the latter of which was predominantly assimilated by komatiites. Both crustal and komatiite-hosted sulfides were overprinted by granite-related skarn alteration during later basin inversion. Spatial S isotopes correlation revealed that Ni mineralisation in komatiites predominantly formed < 5 km from their crustal S sources, excluding long lateral transport as the main metal enrichment mechanism. Rather, metal enrichment likely happened through multiple cycles of sulfide entrapment and entrainment in lava flow vortices that formed in the wake of topographic steps represented by syn-rift faults. These faults were the main loci for pre-existing crustal weaknesses, hydrothermal fluid circulation, and VMS-style sulfide deposition, which were subsequently utilised by komatiites for enhanced thermo-mechanical erosion and crustal sulfide assimilation. This study shows that proximity to the syn-rift faults was the dominant control on the formation of komatiite-hosted Ni–sulfide mineralisation, regardless of substrate lithology. The S isotope signatures of crustal sulfides may be used as a proxy to identify syn-rift faults in highly deformed terranes.

Keywords Sulfur isotopes · Komatiite · Ni-deposits · VMS · Assimilation · Transport · Syn-rift faults

Introduction

Komatiites formed predominantly in the Archaean Eon from large degrees of partial melting of a mantle plume source (Campbell et al. 1989) and were highly sulfide-undersaturated as they erupted (Mavrogenes and O'Neill 1999). A key implication is that assimilation of additional S through thermomechanical erosion of pre-existing S-bearing crust was a pre-requisite for forming komatiite-hosted Ni–sulfide deposits (Huppert et al. 1984; Robertson et al. 2015b; Barnes et al. 2016). Metal enrichment of the initially barren crustal sulfide liquid further required prolonged suspension and transport in the komatiite silicate melt to enhance chemical equilibration prior to deposition within lava channels (Robertson et al. 2015a; Barnes and Robertson 2019; Yao and Mungall 2021, 2022). Yao and Mungall (2021) highlighted the necessity of prolonged transport by demonstrating a positive correlation between metal tenors of magmatic Ni-sulfides with distance from their crustal S source. Consequently, tracking the crustal S source of komatiite-hosted Ni-sulfides may inform on the transport mechanisms involved in the formation of ore deposits.

In recent years, S isotopes have increasingly been used to trace komatiite-hosted magmatic sulfides back to their

Editorial handling: B. Lehmann

✉ Anne B. Virnes
anne.virnes@research.uwa.edu.au

[1] Centre for Exploration Targeting, School of Earth Sciences, The University of Western Australia, Perth, WA, Australia

[2] Commonwealth Scientific and Industrial Research Organisation, Mineral Resources, Kensington, WA, Australia

[3] School of Earth and Environmental Sciences, The University of Queensland, Brisbane, QLD, Australia

Published online: 16 March 2024

crustal S sources (e.g., Ripley and Li 2003; Bekker et al. 2009; Fiorentini et al. 2012a, b; Konnunaho et al. 2013). Importantly, the signatures of mass-independent fractionation of S isotopes (MIF-S, denoted $\Delta^{33}S$), which is the deviation of $\delta^{33}S$ from the mass-dependent $\delta^{33}S$-$\delta^{34}S$ relationship (e.g., Farquhar et al. 2000), are particularly resistant to post-magmatic geological processes causing mass-dependent fractionation, such as metamorphism and weathering (Sharman et al. 2013; Caruso et al. 2020). Moreover, our recent work showed that komatiite-hosted magmatic sulfides largely preserve the MIF-S isotope signatures of their crustal S sources (Virnes et al. 2023). This is due to the highly sulfide undersaturated nature of the komatiite melt upon emplacement (Mavrogenes and O'Neill 1999), the extremely slow diffusivity of S (e.g., Freda et al. 2005), and the relatively short timeframe for sulfide droplet transport and settlement compared to dissolution in komatiite flows (Barnes and Robertson 2019). The assimilated crust-derived sulfide liquid would continuously dissolve into the komatiite silicate melt until the eventual trapping and deposition as magmatic Ni-sulfides, thereby preventing isotopic exchange and equilibration, and thus leading largely to the preservation of their original MIF-S isotope signatures. This allows for direct comparison between komatiite-hosted Ni-sulfides and the crustal S reservoirs, from which they were derived.

Crustal MIF-S signatures in the Archaean largely originated from photodissociation of atmospheric SO_2 caused by ultra-violet (UV) cosmic radiation in the oxygen-poor atmosphere (Farquhar et al. 2000, 2001; Farquhar and Wing 2003). The UV rays split SO_2 into aerosols of reduced, insoluble, MIF-S-positive elemental S (S_8) and oxidised, water-soluble MIF-S-negative sulfate (H_2SO_4; Fig. 1; Farquhar et al. 2001; Ono et al. 2003). These two compounds entered different reservoirs in the hydrosphere and lithosphere: Reduced, elemental S was either subsequently incorporated into sedimentary sulfides or oxidised and mixed with the dissolved seawater sulfate, thus diluting the MIF-S signature of the latter; oxidised seawater sulfate got thermochemically (TSR) or bacterially (BSR) reduced and precipitated as sedimentary sulfides, or as evaporitic or exhalative sulfides in cherts, banded iron formation (BIF), and volcanogenic massive sulfide (VMS) reservoirs (e.g., Canfield 2001; Ono et al. 2003; Farquhar et al. 2013). The resulting sulfide-bearing rocks formed a lateral continuum between rift-distal, dominantly MIF-S positive sedimentary environments and rift-proximal, dominantly MIF-S negative hydrothermal environments (Ono et al. 2003; Fig. 3 in Bekker et al. 2009). However, overlap exists between these different environments and the S sources that sulfides from each environment incorporates, which complicates the interpretation of sulfide formation based solely on their $\Delta^{33}S$ signatures. For example, VMS sulfides that formed from thermochemical reduction of seawater sulfate would have

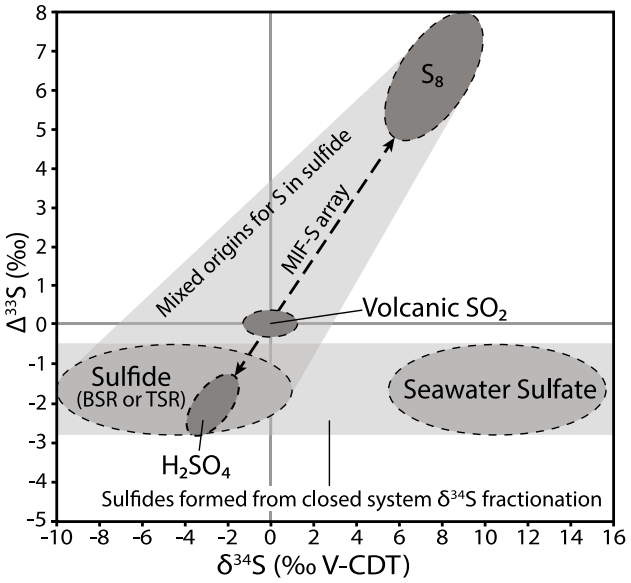

Fig. 1 $\delta^{34}S$-$\Delta^{33}S$ plot of the reduced, insoluble S (S_8) and oxidised, water-soluble sulfate (H_2SO_4) MIF-S reservoirs formed by photodissociation of volcanic SO_2 gas in the Archaean oxygen-free atmosphere (dark grey ovals). Sulfides may form from bacterial (BSR) or thermochemical sulfate reduction (TSR) of dissolved seawater sulfate (light grey ovals) or from oxidation/reduction of the reduced, insoluble S, or a combination of both. Modified from Ono et al. (2003)

similar $\Delta^{33}S$ signatures as e.g., shale-hosted pyrite nodules that formed from bacterial reduction of seawater. On the other hand, sulfides forming from similar processes and in similar environments but incorporating S from different S sources would falsely give the impression that these formed from different processes and were genetically unrelated. It is therefore crucial to establish the environment of sulfide formation based on textural analysis and host rock facies analysis prior to linking $\Delta^{33}S$ isotopic signatures to distinct sulfide occurrences. The $\Delta^{33}S$ signatures can then further inform on the S sources, environment, and chemical conditions of formation.

The application of detailed sulfide textural analysis, host rock or associated alteration facies analysis as well as S isotope analysis to distinct sulfide occurrences in Archaean crustal rocks should therefore enable the evaluation of their formation environments. Furthermore, by characterising komatiite-hosted Ni-sulfides and comparing them to crustal sulfides in the stratigraphic footwall of komatiites, komatiite-hosted Ni–sulfide mineralisation may be spatially linked to their potential crustal S sources. To test this hypothesis, we focus on one of the largest and better constrained komatiite-hosted Ni–sulfide mineralised camps in the Yilgarn Craton of Western Australia, the Agnew-Wiluna Greenstone Belt. We have conducted detailed sulfide textural and facies analysis and generated a comprehensive multiple S isotope database to fingerprint Late Archaean S reservoirs in the region

and to compare them to known Ni–sulfide mineralisation in komatiites. The results are integrated with the extensive body of tectono-stratigraphic and geochronological knowledge accumulated over the past four decades in the region. This in turn allows for a holistic approach to evaluate the transport mechanism and preferred depositional environment of assimilated crustal sulfides in komatiites.

Regional geology

The Agnew-Wiluna Greenstone Belt (AWB) is located in the northern part of the Kalgoorlie Terrane of the Eastern Goldfields Superterrane (Fig. 2a; Cassidy et al. 2006; Pawley et al. 2012). It comprises a ca. 2720–2655 Ma supracrustal succession representing rift-related magmatism and sedimentation followed by exhumation and basin inversion of the Kalgoorlie-Kurnalpi Rift (KKR; Hayman et al. 2015; Gole et al. 2019; Witt et al. 2020; Masurel et al. 2022). Enclaves of ca. 2825–2740 Ma crust have locally been identified across the AWB and imply that the KKR failed and did not reach oceanic spreading stage (Gole et al. 2019; Witt et al. 2020; Masurel et al. 2022). Masurel et al. (2022) recently compiled constraints on the stratigraphic record in the AWB from published/public literature and provided a revised model that includes five distinct cycles (Fig. 2b), which are detailed hereafter in chronological order:

- ca. 2825–2740 Ma Cycle 1, consisting of the Butchers Well Basalt, Donegal Komatiite, Hickies Bore Basalt, Songvang Basalt, and co-magmatic mafic–ultramafic intrusions. The specific tectonic setting of such a stratigraphic package in the AWB remains elusive but it was temporally associated with lithospheric thinning and formation of the Cue Rift in the Youanmi Terrane;
- ca. 2740–2720 Ma Cycle 2, consisting of felsic volcanic and volcaniclastic rocks of the Cosmos Dacite, felsic plutonic rocks, and coeval mafic–ultramafic rocks of the Kathleen Valley Layered Intrusive Complex. The geodynamic trigger for this stratigraphic cycle remains debated but may be linked to (i) docking of the Narryer Terrane against the Youanmi Terrane following embryonic subduction processes, or (ii) impingement of a mantle upwelling and extensive melting at the base of the crust;
- ca. 2720–2690 Ma Cycle 3 started with early bimodal volcanism represented by the Never Can Tell Basalt, and contemporaneous Mount Keith Dacite, followed by eruption of the Agnew-Mount Keith Komatiite, Burrell Well Basalt, Redeemer Basalt and White Hope Basalt, in stratigraphic order. In the Cosmos region, the lowermost units of this stratigraphic cycle (i.e. Never Can Tell Basalt and Mount Keith Dacite) are absent (non-deposition vs. preservation) and the Agnew-Mount Keith Komatiite directly overlies the Cosmos Dacite of Cycle 2 or the Hickies Bore Basalt of Cycle 1;
- ca. 2690–2665 Ma Cycle 4, consisting of the felsic volcano-sedimentary Vivien Formation, Halfway Well Basalt and co-magmatic dyke and sills, as well as the conglomerate, sandstones, and argillites of the Maria Mine Formation. This cycle is interpreted to reflect a gradual switch back to convergent tectonics following the eruption of the Kalgoorlie Large Igneous Province, progressive uplift, and exhumation due to granite doming;
- ca. 2665–2655 Ma Cycle 5, consisting of the Scotty Creek Formation and lateral equivalent Jones Creek Formation, which comprise polymictic conglomerates interbedded with sandstones. This cycle is interpreted to reflect molasse deposition in an intramountain basin adjacent to the Waroonga Shear Zone.

Komatiites, source of S, and Ni mineralisation in the Agnew-Wiluna Greenstone Belt

The Agnew-Wiluna Greenstone Belt (AWB) is host to some of the largest komatiite-hosted Ni deposits in the world, such as the Mount Keith MKD5 (Fig. 3a) and Perseverance Ni deposits (Fig. 3c), along with several smaller deposits and occurrences. Most of the Agnew-Mount Keith Komatiite cooling units hosting economic Ni mineralisation were emplaced within or on top of felsic volcanic-volcaniclastic rocks of the Mount Keith Dacite. This includes the Mount Keith Ultramafic unit (UMK; Fig. 3a) that hosts the disseminated sulfide style MKD5 Ni deposit. Conversely, only a few Ni deposits have been discovered in komatiite units overlying mafic volcanic substrates of the Never Can Tell Basalt. This includes the Cliffs Ultramafic unit (UCL; Fig. 3a) that hosts the basal massive sulfide style Cliffs Ni deposit (e.g., Fiorentini et al. 2010, 2012b).

The felsic volcanic-volcaniclastic substrate to the komatiites hosts several lenses of sulfidic BIF and semi-massive to massive Fe-rich, Cu–Zn-Pb-poor to barren sulfides akin to VMS. Previous studies suggested that these barren VMS were the major crustal S source for the komatiite-hosted Ni deposits in the AWB (Bekker et al. 2009; Fiorentini et al. 2012b). The same authors argued that sulfidic and carbonaceous interflow sediments in the mafic volcanic substrate comparatively appear to have contributed little to the S budget associated with ore formation. It was therefore inferred that felsic-hosted komatiite systems in bimodal settings were more prospective for Ni deposits than their mafic counterparts (Fiorentini et al. 2012b).

Felsic volcanic rocks and associated MIF-S negative sulfidic BIF and VMS in rift settings predominantly formed proximal to the rift axis, while mafic volcanic and MIF-S positive sulfidic sedimentary rocks dominated in distal

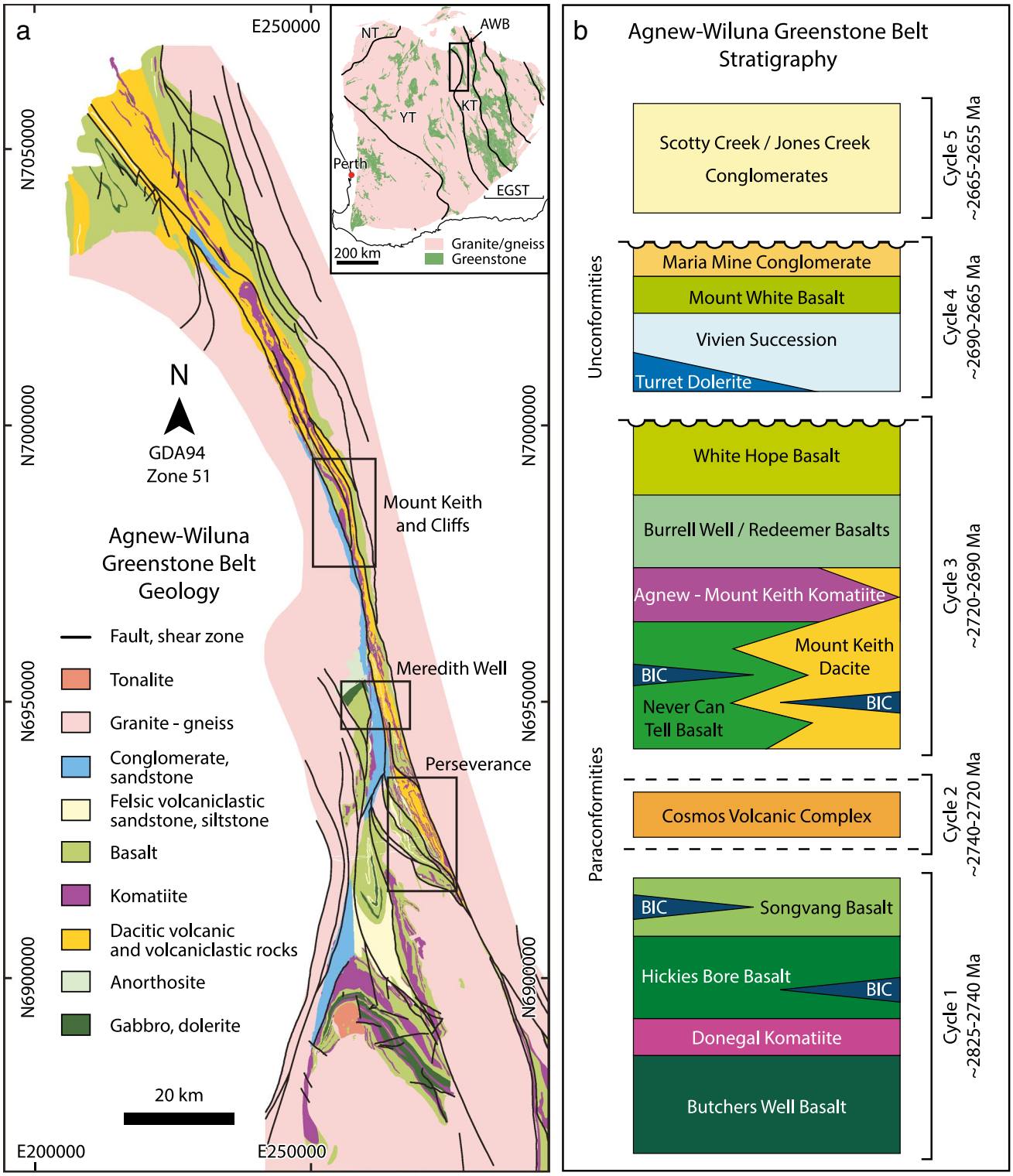

Fig. 2 Regional geology and stratigraphy of the Agnew-Wiluna Greenstone Belt. a) Simplified geological map, modified from Beresford et al. (2004). Inset is a granite-greenstone map of the Yilgarn Craton, modified from Martin et al. (2015) with terrane boundaries after Cassidy et al. (2006) and Pawley et al. (2012). Boxes show the regions studied in this project. b) Agnew-Wiluna Greenstone Belt stratigraphy, modified from Masurel et al. (2022). Abbreviations: AWB = Agnew-Wiluna Greenstone Belt, EGST = Eastern Goldfields Super Terrane; KT = Kalgoorlie Terrane; NT = Narryer Terrane; YT = Youanmi Terrane; BIC = Bounty Igneous Complex; MKD = Mount Keith Dacite

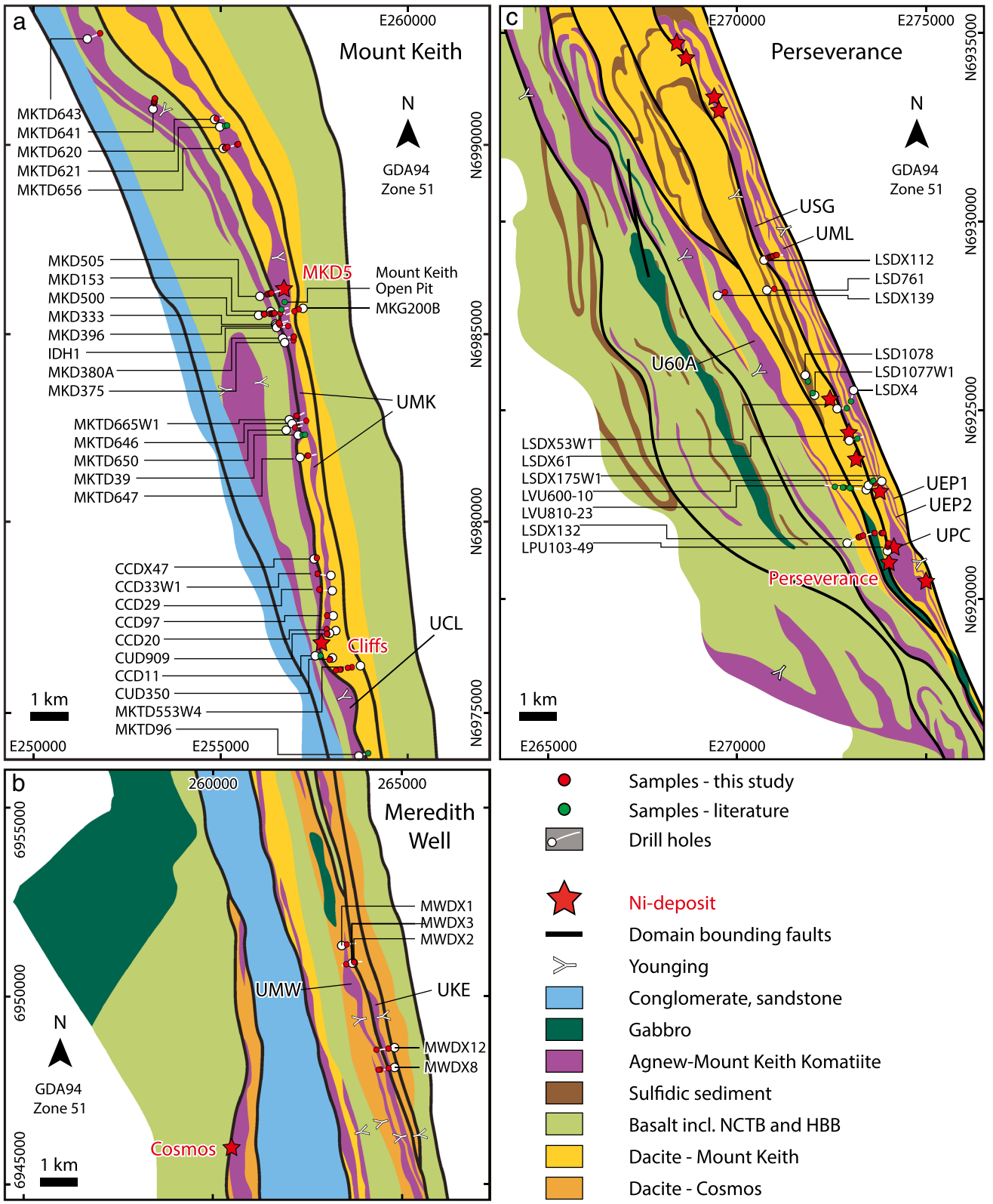

Fig. 3 Geology of a) the Mount Keith region, b) Meredith Well region, and c) Perseverance region (modified from Perring 2015a, b, 2016), with locations of drill holes and samples. Abbreviations: HBB = Hickies Bore Basalt; NCTB = Never Can Tell Basalt; UCL = Cliffs Ultramafic unit; UEP1 = East Perseverance 1 Ultramafic unit; UEP2 = East Perseverance 2 Ultramafic unit; UKE = Kathleen East Ultramafic unit; UMK = Mount Keith Ultramafic unit; UML = Merlin Ultramafic unit; UMW = Meredith Well Ultramafic unit; UPC = Perseverance Ultramafic Complex; USG = Sir Gawain Ultramafic unit; U60A = Sixty A Ultramafic unit

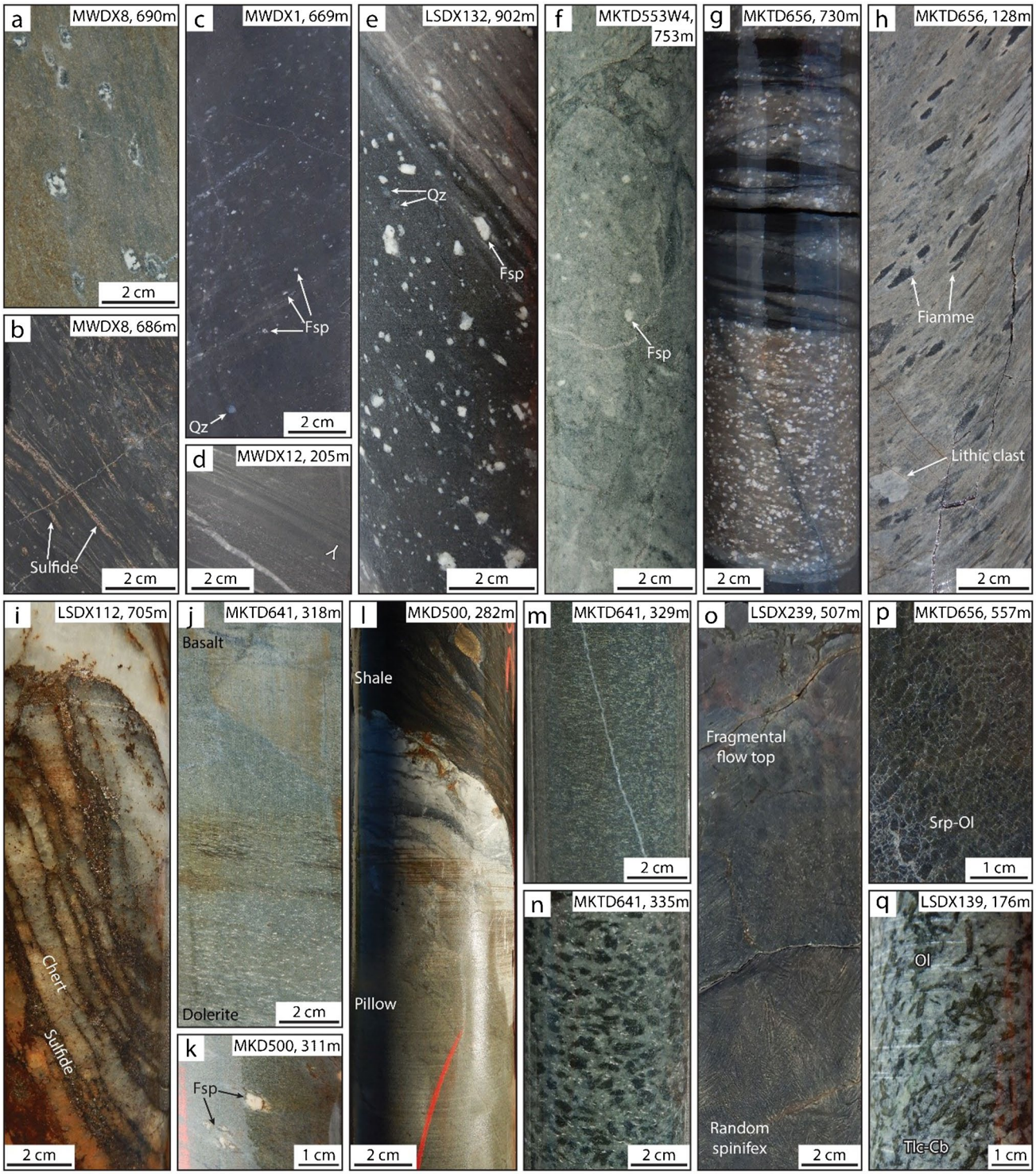

environments (e.g., Herzig and Hannington 1995; Bekker et al. 2009, 2010; Wanless et al. 2010). Negative MIF-S isotopic signatures of the MKD5 and Cliffs Ni deposits suggested that they both sourced rift-proximal VMS-style sulfides (Bekker et al. 2009; Fiorentini et al. 2012b). A matching Fe-rich, Cu–Zn-Pb-barren VMS-style crustal S source for the MKD5 Ni deposit was located in the immediate felsic footwall rocks to the Mount Keith Ultramafic unit at the site of the deposit. This suggested that sulfide assimilation and deposition for the MKD5 Ni deposit occurred proximal to the rift and the VMS-style crustal S source (Fiorentini et al. 2012b). In contrast, the S-isotopes of the Cliffs Ni deposit did not match the sulfides in the mafic footwall rocks to the Cliffs Ultramafic unit at the site of the

◂**Fig. 4** Core photos of rocks from the Agnew-Mount Keith Komatiite and its stratigraphic substrate. Figures a-b are from the Hickies Bore Basalt, c-d are from the Cosmos Dacite, e-i are from the Mount Keith Dacite, j-n are from the Never Can Tell Basalt, and o-q are from the Agnew-Mount Keith Komatiite. **a**) Altered amygdaloidal basalt. **b**) Sulfidic interflow mudstone. **c**) Feldspar and quartz crystal rich sandstone interpreted as resedimented pyroclastic rock. **d**) Graded bedding in resedimented pyroclastic rock. **e**) Strained, feldspar-quartz-porphyritic coherent dacite. **f**) Monomict feldspar-quartz-porphyritic dacitic clast supported breccia interpreted as in-situ hyaloclastite gradational to coherent dacite. **g**) Strained, monomict feldspar-quartz-porphyritic dacitic pebble to cobble matrix supported breccia interpreted as resedimented hyaloclastite. **h**) Strained, fiamme-rich sandstone with lithic clasts interpreted as resedimented pyroclastic rock. **i**) Sulfidic chert. **j**) Massive basalt grading into dolerite facies. **k**) Feldspar-porphyritic massive basalt. **l**) Sulfidic shale conformably overlying chilled, bleached pillow basalt. **m**) Dolerite facies. **n**) Gabbro facies. **o**) Fragmental flow top facies grading to random spinifex textured komatiite. **p**) Serpentinised olivine-adcumulate retaining the original magmatic texture. **q**) Cumulate facies komatiite metamorphosed to amphibolite facies with a completely recrystallised jackstraw texture of bladed green olivine in a fine-grained talc-carbonate matrix. Abbreviations: Cb = carbonate; Fsp = feldspar; Ol = olivine; Qz = quartz; Srp = serpentine; Tlc = talc

deposit. This indicated that magmatic Ni-sulfides from the Cliffs Ni deposit had been transported and emplaced distal from the rift and the VMS-style crustal S source (Fiorentini et al. 2012b).

However, according to the findings of Yao and Mungall (2021) that metal tenors of magmatic Ni-sulfides are positively correlated with distance from source, the Cliffs Ni deposit should have higher metal tenors than the MKD5 Ni deposit. But, Perring (2015b) reported similar metal tenors for both deposits, and based on structural analysis, identified the intersection of proposed early growth faults as the potential volcanic vents < 2 km from either ore body. Perring (2015b) also reported barren VMS-style lenses in the mafic volcanic footwall to the Cliffs Ni deposit, which were proposed to have been the crustal S source for Cliffs. These VMS-style sulfides had not been analysed for S isotopes until now and could therefore not be confirmed as the crustal S source for the Cliffs Ni deposit. However, in contrast to the distal model for Cliffs Ni deposit (Fiorentini et al. 2012b), the evidence provided by Perring (2015b) suggested that, similar to the MKD5 Ni deposit, the Cliffs Ni deposit also formed proximal to the rift and a VMS-style crustal S source. Thus, the prospectivity of mafic-hosted komatiites in bimodal settings needs to be re-evaluated.

Materials and methods

In order to evaluate the crustal sulfide reservoirs and their spatial relationship(s) with komatiite-hosted Ni-mineralisation in the AWB, we collected 109 samples from 35 drill cores from the Mount Keith (Fig. 3a), Meredith Well (Fig. 3b), and Perseverance regions (Fig. 3c). These samples represent magmatic Ni-sulfides from the Agnew-Mount Keith Komatiite as well as sedimentary and hydrothermal sulfide-bearing lithologies in the lower Cycle 3 bimodal mafic and felsic volcanic-volcaniclastic footwall stratigraphic units of the Never Can Tell Basalt and Mount Keith Dacite. In the Meredith Well region (Fig. 3b), where these units are proposed to be missing, we sampled the Cycle 1 Hickies Bore Basalt and a felsic volcaniclastic unit proposed to be the Cycle 2 Cosmos Dacite. These stratigraphic footwall units as well as the Agnew-Mount Keith Komatiite are briefly described below from oldest to youngest.

Stratigraphic units and samples

Hickies Bore Basalt

The Hickies Bore Basalt is an up-to-1.5 km thick high-Mg, low-Th tholeiite succession consisting of massive and pillowed, locally amygdaloidal basalt (Fig. 4a) with intervening dolerite-gabbro sills, some of which contain minor mafic–ultramafic cumulates (Liu et al. 1996; Hayman et al. 2015). The Hickies Bore Basalt is interpreted to represent submarine pillow and sheet flows with differentiated co-magmatic intrusions, which was subsequently metamorphosed to upper-greenschist to amphibolite-facies conditions (Liu et al. 1996; Hayman et al. 2015). Although undated, a minimum age of at least 2750 Ma is inferred for the Hickies Bore Basalt based on SHRIMP U–Pb dating of zircons from a microdiorite dyke in the Wiluna region (Kent and Hagemann 1996). This dyke crosscuts a basalt unit that has been chemostratigraphically correlated with the Songvang Basalt in the Agnew region, the latter of which stratigraphically overlies the Hickies Bore Basalt (Gole et al. 2019). Several felsic volcanic interlayers as well as sulfidic interflow mudstones (Fig. 4b) have been reported from the Hickies Bore Basalt (Liu et al. 1996; Hayman et al. 2015). One sample of basalt and two samples of sulfidic interflow shale were collected from the Hickies Bore Basalt in the Meredith Well region (Fig. 3b).

Cosmos Dacite

The Cosmos Dacite consists of high-K calc-alkaline to shoshonitic quartz-feldspar-porphyritic dacitic to rhyolite lavas or lava domes, basaltic-andesitic amygdaloidal lavas, associated autoclastic and fragmental horizons, and lapilli and crystal-bearing tuffs (Fig. 4c-d; Kaye et al. 2010; de Joux et al. 2013, 2014). A sequence of andesite lavas intercalated with dacite lavas and dacitic lapilli tuffs forms the immediate stratigraphic substrate to the Ni-mineralised Cosmos Ultramafic Sequence (de Joux et al. 2013). The succession was constrained to ca. 2740–2720 Ma by SIMS U–Pb on zircon,

and all units are deformed and metamorphosed to amphibolite-facies conditions (de Joux et al. 2013; de Joux 2014). Submarine sedimentary rocks and S-bearing horizons have not been observed in the Cosmos Dacite (Kaye et al. 2010; de Joux et al. 2013, 2014). Two samples of sulfide-bearing crystal-rich siltstone of dacitic composition and one sample of sulfide-bearing shale were collected from the proposed Cosmos Dacite in the Meredith Well region (Fig. 3b).

Mount Keith Dacite

The Mount Keith Dacite consists of dacitic to rhyodacitic, feldspar- and quartz-porphyritic, amygdaloidal coherent (Fig. 4e), autoclastic (Fig. 4f-g) and minor pyroclastic volcanic rocks (Fig. 4h) with trondhjemite-tonalite-dacite geochemical affinity, interlayered with deep subaqueous carbonaceous and sulfidic shale, mudstone and chert (Trofimovs et al. 2003; Rosengren et al. 2008; Fiorentini et al. 2012b). These facies have collectively been interpreted as (i) multiple laterally extensive lava flows with hyaloclastite rims and resedimented pyroclastic deposits in the Mount Keith region (Rosengren et al. 2008) in contrast to (ii) shallow intrusive lavas in the Perseverance region (Trofimovs et al. 2003). The Mount Keith Dacite was dated at ca. 2719–2700 Ma by SHRIMP U–Pb on zircon and titanite, with an inherited component dated at 2740–2730 Ma (Fiorentini et al. 2005). The rocks underwent syn-volcanic hydrothermal alteration and mid-greenschist-facies metamorphism in the Mount Keith region (Rosengren et al. 2008), and amphibolite-facies metamorphism in the Perseverance region (Archibald et al. 1978). Besides the sulfidic shale and chert, centimetre- to metre-scale lenses of semi-massive to massive Fe-rich, Cu–Zn-Pb-poor to barren sulfides have been identified and interpreted to represent sulfidic BIF and syn-volcanic mineralisation akin to VMS (Fig. 4i; Bekker et al. 2009; Fiorentini et al. 2012b; C. Isaac, unpub. PhD thesis, 2015; Perring 2015a, b, 2016; E. Lewis, unpub. BSc (Hons) thesis, 2019). We collected 29 samples of hydrothermally altered and sulfide-bearing coherent and volcaniclastic dacite, six samples of sulfidic chert and hydrothermal breccia, two samples of Cu–Zn-Pb-poor massive sulfide lenses, and one sample of sulfidic shale from the Mount Keith Dacite in the Mount Keith and Perseverance regions (Fig. 3a, c).

Never Can Tell Basalt

The Never Can Tell Basalt is ca. 300 m thick in the least deformed south-western part of the AWB and is a low- to moderately crustal contaminated, highly fractionated high-Fe-Ti tholeiite (Hayman et al. 2015; Gole et al. 2019). It comprises a variably aphyric (Fig. 4j) to plagioclase-porphyritic (Fig. 4k) massive and locally pillowed basalt (Fig. 4l), with minor dolerite-gabbro units (Fig. 4m-n), metamorphosed to greenschist to amphibolite facies (Liu et al. 1996; Hayman et al. 2015; Gole et al. 2019). It is interpreted to represent deep submarine massive sheet flows based on several thin deep-subaqueous mudstone and shale intervals. A tuffaceous interflow bed was dated by SHRIMP U–Pb at 2711 ± 4 Ma (Hayman et al. 2015). S-bearing lithologies in the Never Can Tell Basalt include sulfidic shales (Fig. 4l) as well as VMS-style massive Fe-rich sulfides (Bekker et al. 2009; Fiorentini et al. 2012b; Hayman et al. 2015; Perring 2015a, b, 2016). We collected 23 samples of hydrothermally altered and sulfide-bearing coherent and minor fragmental basalt and dolerite, 11 samples of sulfidic interflow shale and siltstone, and five samples of sulfidic chert from the Never Can Tell Basalt in the Mount Keith region (Fig. 3a).

Agnew-Mount Keith Komatiite

The Agnew-Mount Keith Komatiite is an Al-undepleted (Munro-type) komatiite with parental magma MgO of 25–33 wt.% (e.g., Naldrett and Turner 1977; Barnes et al. 1988), displaying trace-element evidence for varying degrees of crustal contamination (Fiorentini et al. 2010). It comprises several cooling units ranging from thin, metre-scale spinifex-textured differentiated lava flows (Fig. 4o), to several-hundred-metres thick, massive, and cumulate-rich channelised sheet lava flows, and sheets and lenticular bodies of dunite (Fig. 4p), some of which are interpreted as intrusive feeder sills (e.g., Naldrett and Turner 1977; Hill et al. 1995; Rosengren et al. 2005; Fiorentini et al. 2012b). The komatiite was dated at 2705 ± 36 Ma by Re-Os in magmatic sulfide ores (Foster et al. 1996), in agreement with bracketing U–Pb ages from the under- and overlying Mount Keith Dacite (Fiorentini et al. 2005). The komatiite is extensively serpentinised (Fig. 4p) and/or talc-carbonate altered and metamorphosed to prehnite-pumpellyite facies in the northern part and amphibolite facies in the southern part of the AWB (Fig. 4q; Archibald et al. 1978; Gole et al. 1987). Magmatic Ni–sulfide mineralisation occurs predominantly in the most magnesian, cumulate facies and crustal contaminated komatiites (Barnes and Fiorentini 2012), either as centimetre-to-metre-scale basal massive and net-textured mineralisation or as large, up to several-hundred-metre-scale, lenticular disseminations (e.g., Fiorentini et al. 2012b and references within). We collected 15 samples of magmatic Ni–sulfide mineralisation from the Agnew-Mount Keith Komatiite in the Mount Keith region (Fig. 3a), three samples from the Meredith Well region (Fig. 3b), and eight samples from the Perseverance region (Fig. 3c).

Petrography

All samples were described focusing on lithology, deformation, style and relative timing of sulfides and associated

hydrothermal alteration, if present. The samples were categorised based on the sulfide paragenesis and representative polished thin sections of all sulfide and alteration parageneses were produced and described using transmitted and reflected light microscopy at the School of Earth Sciences, University of Western Australia (UWA). Backscatter electron (BSE) imaging and semi-quantitative chemical analysis of mineral phases were obtained at 15 kV, 0.8 nA at a 5.5 mm working distance using a FEI Verios 460 scanning electron microscope (SEM) fitted with an Oxford Instruments X-Max energy dispersive X-ray spectrometer (EDS), located at the Centre for Microscopy, Characterisation and Analysis (CMCA) at UWA. The polished thin sections were coated with 20 nm carbon.

Multiple S isotopes by EA-IRMS

Following petrographic description, 1–3 sulfides per sample were marked for drilling prior to S isotope analysis. Care was taken to select sulfide grains or aggregates large enough for Elemental Analyser—Isotope Ratio Mass Spectrometry (EA-IRMS) analysis while remaining as uncontaminated by other parageneses or as undiluted by silicates as possible. S isotope analysis was carried out at the Stable Isotope Geochemistry Laboratory at the University of Queensland following a modified procedure described in Baublys et al. (2004).

The selected sulfide grains from each of the samples were drilled out immediately prior to analysis, combusted at 1150°C in an Elementar Vario Isotope Cube elemental analyser in S-only mode, and passed through a PrecisION isotope ratio mass spectrometer. The $\delta^{34}S$ and $\delta^{33}S$ ratios were determined simultaneously by focusing on the SO fragment ions (mass ratios of 50/48 and 49/48) produced in the source from SO_2. Drift correction was performed when required on all standards and unknowns using in-house MIF-S laboratory pyrite check standard WD-11. The $\delta^{34}S$, $\delta^{33}S$, and $\Delta^{33}S$ values and 2σ uncertainties for WD-11 throughout all analysis sessions were $+3.68 \pm 0.23‰$, $+1.38 \pm 0.26‰$, and $-0.51 \pm 0.27‰$, respectively. After drift correction, a three-point normalisation calibration was performed for each analysis session using international silver sulfide standards IAEA–S1, S2, and S3 analysed at the beginning, the middle and at the end of each run. $\delta^{34}S_{V\text{-}CDT}$ values for standards IAEA-S1, S2, and S3 were -0.3‰, +22.64‰, and -32.3‰, respectively, and $\delta^{33}S_{V\text{-}CDT}$ values were -0.05‰, +11.65‰, and -16.56‰, respectively (Ding et al. 2001).

Each sample was analysed in duplicate and repeated if the results differed by $> \pm 0.5‰$. Results of $\delta^{34}S$ and $\delta^{33}S$ were normalised to V-CDT (Ding et al. 2001), and measurement precision of $\delta^{34}S$ and $\delta^{33}S$ values were calculated as the pooled 2σ standard deviation of the calibration standards (and check standard, if no drift correction was performed) for each analytical session (Szpak et al. 2017). Pooled 2σ uncertainties varied from $\pm 0.16‰$ to $\pm 0.74‰$ for $\delta^{34}S$, and from $\pm 0.15‰$ to $\pm 0.50‰$ for $\delta^{33}S$. $\Delta^{33}S$ values were calculated using the method outlined in Farquhar and Wing (2003), and the corresponding uncertainties, varying from $\pm 0.19‰$ to $\pm 0.63‰$ at 2σ, were propagated using the uncertainties in $\delta^{34}S$ and $\delta^{33}S$. Data for sample averages, unknowns and standards are provided in supplementary material (ESM1).

Results

Five different sulfide assemblages with their related alteration styles are identified in the sample set. These are (1) pyrrhotite-pyrite ± sphalerite ± chalcopyrite ± galena in metasediment (Fig. 5a-d); (2) pyrrhotite-pyrite-magnetite ± chalcopyrite in chert (Fig. 5e-h); (3) pyrrhotite-pyrite ± sphalerite ± chalcopyrite ± galena related to quartz-carbonate-albite-sericite-chlorite-biotite alteration in basalt and dacite (Fig. 5i-n); (4) pyrrhotite-pyrite-magnetite ± chalcopyrite ± pentlandite related to quartz-carbonate-garnet-amphibole-pyroxene-biotite alteration in basalt, dacite, and komatiite (Fig. 5o-q); and (5) pyrrhotite-pentlandite ± chalcopyrite in serpentinised and talc-carbonate altered komatiite (Fig. 5r-u). Characteristics of the sulfide assemblages and their related alteration styles are summarised in Table 1 with detailed descriptions provided in supplementary material (ESM2). Of the total of 109 samples, 105 samples yielded S isotope results through EA-IRMS analysis. These are also summarised in Table 1 and plotted in Fig. 6 together with literature data.

The sulfides from metasediments generally plot along the mixing field between the two MIF-S reservoirs with elemental S as the dominant source. Most sulfides in chert and sulfides in the quartz-carbonate-albite-sericite-chlorite-biotite altered samples and all quartz-carbonate-garnet-amphibole-pyroxene-biotite altered samples plot in the upper part of the negative MIF-S field with seawater sulfate as the dominant S source. These also show a large spread in $\delta^{34}S$ between the reservoirs of seawater sulfate and sulfide produced from bacterial or thermochemical sulfate reduction (BSR or TSR).

The isotope signatures of sulfides in the altered komatiites generally plot in the negative MIF-S field and consistently overlap with those of the sulfidic cherts, the sulfides related to the quartz-carbonate-albite-sericite-chlorite-biotite alteration, the sulfides related to the quartz-carbonate-garnet-amphibole-pyroxene-biotite alteration as well as the VMS and BIF sulfides from the literature. Some overlap exists between the sulfides in altered komatiite and those in the metasediments; however, it is significantly less in terms of $\Delta^{33}S$ compared to the other groups.

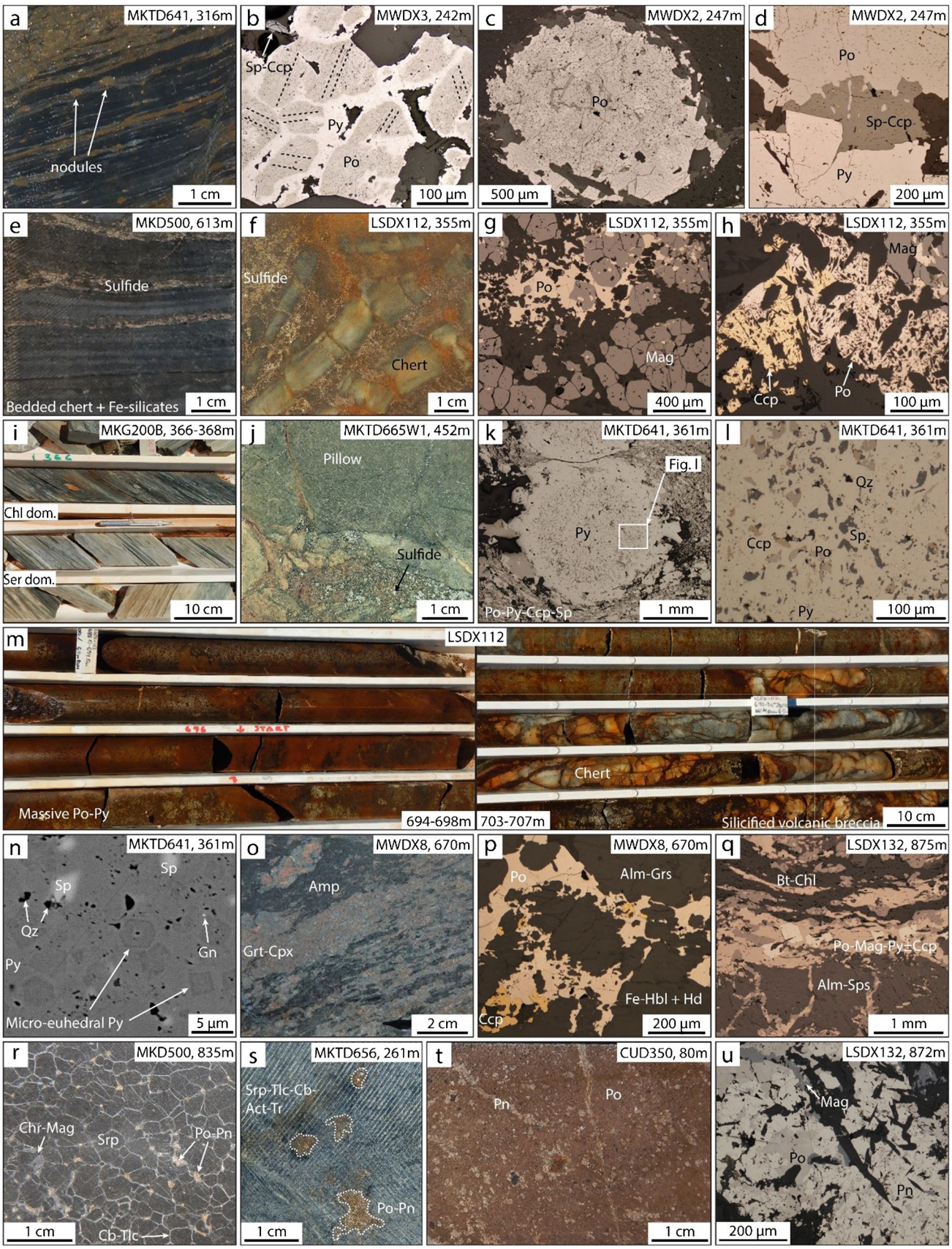
a
MKTD641, 316m
nodules
1 cm
b
MWDX3, 242m
Sp-Ccp
Py
Po
100 µm
c
MWDX2, 247m
Po
500 µm
d
MWDX2, 247m
Po
Sp-Ccp
Py
200 µm
e
MKD500, 613m
Sulfide
Bedded chert + Fe-silicates
1 cm
f
LSDX112, 355m
Sulfide
Chert
1 cm
g
LSDX112, 355m
Po
Mag
400 µm
h
LSDX112, 355m
Mag
Ccp
Po
100 µm
i
MKG200B, 366-368m
Chl dom.
Ser dom.
10 cm
j
MKTD665W1, 452m
Pillow
Sulfide
1 cm
k
MKTD641, 361m
Fig. l
Py
Po-Py-Ccp-Sp
1 mm
l
MKTD641, 361m
Qz
Ccp
Sp
Po
Py
100 µm
m
LSDX112
Massive Po-Py
694-698m
703-707m
Chert
Silicified volcanic breccia
10 cm
n
MKTD641, 361m
Sp
Sp
Qz
Gn
Py
Micro-euhedral Py
5 µm
o
MWDX8, 670m
Amp
Grt-Cpx
2 cm
p
MWDX8, 670m
Po
Alm-Grs
Fe-Hbl + Hd
Ccp
200 µm
q
LSDX132, 875m
Bt-Chl
Po-Mag-Py±Ccp
Alm-Sps
1 mm
r
MKD500, 835m
Chr-Mag
Srp
Po-Pn
1 cm
Cb-Tlc
s
MKTD656, 261m
Srp-Tlc-Cb-
Act-Tr
Po-Pn
1 cm
t
CUD350, 80m
Pn
Po
1 cm
u
LSDX132, 872m
Mag
Po
Pn
200 µm

◂**Fig. 5** Core photos (figs. a, e–f, i-j, m, and r-s), reflected light photomicrographs (figs. b-d, g-h, k-l, p-q, and u), and BSE-image (fig. n) of sulfide assemblages and alteration styles. **a**) Bedding-parallel sulfide laminae and nodules in metashale. **b**) Resedimented clasts of laminated pyrrhotite with varying orientations of the internal laminations (dashed lines) in metasiltstone. The clasts are overgrown and cemented by later inclusion-free, idiomorphic pyrite. **c**) Spongy pyrrhotite nodule with abundant inclusions of organic matter in metasiltstone. **d**) Intergrown spongy pyrrhotite-pyrite-sphalerite full of inclusions of organic matter in metasiltstone. Sphalerite displays chalcopyrite-exsolutions. **e**) Chert with abundant darker, carbonaceous, and Fe-silicate-rich, magnetite- and sulfide-bearing laminae. **f**) Deformed sulfidic chert with ductile sulfides remobilised in between brecciated brittle chert clasts. **g**) Granular and inclusion-rich magnetite with anhedral masses of pyrrhotite in sulfidic chert. Magnetite and pyrrhotite display mutual inclusions. **h**) Inclusion-rich pyrrhotite and chalcopyrite intergrown with Fe-silicates in chert. **i**) Transition from chlorite-dominated to sericite-dominated alteration in highly strained, quartz-carbonate-sericite-chlorite-biotite altered, coherent volcanic dacite. **j**) Sulfide-carbonate filling of interpillow space and cooling fractures in carbonate-quartz-chlorite altered basalt. **k**) Porphyroclastic spongy pyrite nodule filling a relict amygdale in quartz-carbonate-chlorite-sericite-biotite altered basalt. Abundant inclusions of, and surrounded by, fine grained masses of pyrrhotite, pyrite, sphalerite, chalcopyrite, and galena, which are flattened along the foliation and wrap around the nodule. **l**) Close-up of inclusions in k. **m**) More than 10 m thick semi-massive to massive pyrrhotite-pyrite dominated sulfides replacing hyaloclastic dacite and interlayered with chert. **n**) High-contrast BSE-image of spongy pyrite nodule in altered basalt showing micro-euhedral pyrite grains intergrown with sphalerite and galena. The sphalerite and galena intergrown with the microeuhedral pyrite are replaced by later pyrite, as evidenced by the diffuse and irregular boundaries between the latter and sphalerite. **o**) Intense banded garnet-clinopyroxene-amphibole alteration in basalt or dolerite. **p**) Pyrrhotite-chalcopyrite intergrown with almandine-grossular-Fe-hornblende-hedenbergite alteration assemblage in basalt or dolerite. **q**) Highly deformed bands of pyrrhotite-magnetite-chalcopyrite with idiomorphic pyrite, intergrown with almandine-spessartine-biotite, the latter being partially replaced by chlorite, in intensely altered dacite. **r**) Serpentinised olivine-sulfide adcumulate komatiite with accessory chromite altered to magnetite. **s**) Centimetre-scale irregular and interlobate sulfide blebs in serpentinised and talc-carbonate-actinolite-tremolite altered komatiite. **t**) Basal massive sulfides in komatiite. **u**) Typical sulfide assemblage of pyrrhotite and pentlandite rimmed by minor magnetite in komatiite. Abbreviations: Act = actinolite, Alm = almandine, Amp = amphibole, Bt = biotite, Cb = carbonate, Ccp = chalcopyrite, Chl = chlorite, Chr = chromite, Cpx = clinopyroxexne, dom = dominated, Gn = galena, Grs = grossular, Grt = garnet, Hbl = hornblende, Hd = hedenbergite, Mag = magnetite, Pn = pentlandite, Po = pyrrhotite, Py = pyrite, Qz = quartz, Ser = sericite, Sp = sphalerite, Sps = spessartine, Srp = serpentine, Tlc = talc, Tr = tremolite

Discussion

In this section, we first discuss the origins of different sulfide assemblages and their relative timing with respect to host rock deposition/emplacement, in order to resolve whether the respective sulfide reservoirs were available for assimilation during komatiite eruption. We also discuss the different depositional environments that these sulfides and their host rocks represent and how they fit into the architecture of a continental rift as the currently proposed geodynamic setting of the AWB (Masurel et al. 2022). Secondly, we take advantage of the sulfide liquid-silicate melt S-isotopic disequilibrium (Virnes et al. 2023) that caused the preservation of the crustal MIF-S signatures of the magmatic Ni-sulfides. This relationship allows for the comparison between the S-isotopic signatures of the magmatic Ni-sulfides and those of the crustal sulfides, which are deemed "available" at the time of komatiite emplacement. This comparison is used to propose the most likely crustal assimilant(s) for the komatiites. Lastly, we establish the spatial relationship between the komatiite-hosted sulfides and their potential crustal S sources to discuss the transport- and metal enrichment mechanisms of crust-derived sulfide liquid in komatiite flows. In the following we apply the term "VMS" in a genetic sense, referring to the process of formation, i.e., sulfides that formed from syn-volcanic hydrothermal venting or subseafloor replacement. However, sulfides interpreted to have formed through such processes are not significantly, if at all, enriched in Cu–Zn-Pb, which is otherwise common for economic VMS mineralisation.

Sulfur reservoirs in the Agnew-Wiluna Greenstone Belt

Sedimentary or early diagenetic sulfides

The presence of sulfidic and carbonaceous shales (Fig. 4b, l; Fig. 5a; ESM2, Fig. 1a-d, g-h) in rock sequences associated with Cycle 2 and early Cycle 3 is indicative of a deep, anoxic to euxinic, relatively stagnant subaqueous depositional environment (Nichols 2009; Rickard 2012). The siltstones similarly formed in a subaqueous environment below storm wave base based on the lack of larger clasts or sedimentary structures, such as hummocks or crossbedding (Fig. 4c-d; ESM2, Fig. 1e-f, i; Nichols 2009). The dispersed feldspar and quartz crystals (Fig. 4c-d; ESM2, Fig. 1e-f) are evidence of a volcaniclastic origin, and the presence of rounded clasts of laminated sulfides (Fig. 5b) further suggests that the metasiltstones represent the very distal fringes of volcaniclastic turbidites (McPhie et al. 1993). The clasts were likely sourced from sedimentary or exhalative sulfides upstream from or at the source of the turbidite and deposited distal to the volcanic centre (McPhie et al. 1993; Nichols 2009). We therefore interpret the facies variations in the metasedimentary rocks to represent a lateral transition from either the fringes of a continental slope or the topographic high of a central rift axis, towards the deeper abyssal plains. This indicates that most of the KKR was deeply submerged during the Cycle 1–3 extension and rifting (Masurel et al. 2022).

Table 1 Summary of sulfide assemblages, related alteration styles, and corresponding S isotope variabilities, averages, and uncertainties

			$\delta^{34}S$ (‰ V-CDT)				$\Delta^{33}S$ (‰)			
Assemblage (number of samples)	Description	Sulfide content and textures	Min	Max	Med	±2σ	Min	Max	Med	±2σ
Po-Py±Sp±Ccp±Gn in metasediment (15)	V.f.g. silt-stone to shale with mm-to-cm-scale graded beds (Fig. 5a; ESM2, Fig. 1a-g). Thin m-scale interflow beds in the HBB and NCTB (Fig. 4b, l), less common in MKD. Up to several 100 m thick units in the CD. Groundmass mineralogy consists of Qz, Fsp, Ser, Chl, Bt, and Gr or Org (ESM2, Fig. 1e-h). Dispersed equant, anhe-dral grains of Qz and Fsp in silty beds (ESM2, Fig. 1f). May contain por-phyroblasts of Alm-Sps (ESM2, Fig. 1f) or And/Crd (ESM2, Fig. 1i). Commonly deformed, chaotically folded, and with rotaded porphyroblasts (ESM2, Fig. 1g, i)	Sulfide content is commonly 1–3 vol.% (ESM2, Fig. 1a-b), locally up to 10 vol.% or more (ESM2, Fig. 1c-d). Occur as bedding-parallel lenses (Fig. 5a; ESM2, Fig. 1a-d), laminae and resedimented clasts (Fig. 5b), nodules (Fig. 5c; ESM2, Fig. 1a-d), and fine dis-seminations, including micro-euhedral Py grains (ESM2, Fig. 1l). Dominated by Po and Py. Sp-Ccp-Gn dominantly identified microscopically. Display spongy and porous textures (Fig. 5b-d) with common mutual inclusions (Fig. 5d) and gangue inclusions. Commonly deformed, flattened, boudinaged or remobilised into bedding cross-cutting stringers (ESM2, Fig. 1c-d). Porphyroclastic nodules with pressure shadows (Fig. 5c). Secondary inclusion-free idiomorphic sulfide overgrowths (Fig. 5b)	-5.62	+4.48	+1.5	≤0.52	-0.17	+3.8	+1.18	≤0.45
Po-Py-Mag±Ccp in chert (8)	Cm-to-m-scale beds (Fig. 5e; ESM2, Fig. 2a-d) commonly located transitional between coherent and autoclastic volcanic facies and interflow mudstone and shale in the NCTB and MKD. Strongly deformed and often brecciated (Fig. 5f; ESM2, Fig. 2a-c). Consists of massive, granoblastic quartzite beds (ESM2, Fig. 2e) interlayered with Fe-silicate-rich (ESM2, Fig. 2f-g), oxide- and/or sulfide-bearing laminae (Fig. 5e; ESM2, Fig. 2h-j). The Fe-silicates are granoblastic to decussate and dominated by Mn-bearing Fe-rich Cum-Gru, Fe-Act, Cpx and Grt (ESM2, Fig. 2f-g). Secondary replacement by Amp-Chl	Sulfide + Mag content vary from < 5 vol.% disseminations, nodules (Fig. 5g; ESM2, Fig. 2a), and bedding-parallel string-ers (Fig. 5e) to m-scale semi-massive to massive sulfides (ESM2, Fig. 2c). Display spongy, inclusion-rich textures with both mutual sulfide-Mag inclusions and gangue inclusions (Fig. 5g). Also intergrown with granoblastic to deccusate Fe-silicates (Fig. 5h; ESM2, Fig. 2f-g). Highly deformed and commonly remobilised between brecciated chert clasts (Fig. 5f; ESM2, Fig. 2a-c)	-4.51	+7.33	-0.72	≤0.52	-0.8	+1.52	-0.46	≤0.45

Table 1 (continued)

Assemblage (number of samples)	Description	Sulfide content and textures	$\delta^{34}S$ (‰ V-CDT)				$\Delta^{33}S$ (‰)			
			Min	Max	Med	±2σ	Min	Max	Med	±2σ
Po-Py ± Sp ± Ccp ± Gn related to Qz-Cb-Ab-Ser-Chl-Bt alteration (49)	Widespread m-scale, locally up to 100 m-scale patchy to pervasive alteration (Fig. 5i) in MKD (ESM2, Fig. 3a-c, h-i) and NCTB (ESM2, Fig. 3d-g), rarely in CD. Not observed in HBB. Alters volcanic-volcaniclastic groundmass and phenocrysts (ESM2, Fig. 3b-c, e–f), and fills interpillow space (Fig. 5j), cooling fractures, and amygdales (Fig. 5k-l; ESM2, Fig. 3g). Commonly strongly deformed and foliated with phenocysts and amygdales flattened and rotated into porphyroclasts with pressure shadows (ESM2, Fig. 3b-c, g, j). Dominated by Qz-Cb-Ab-Ser-Chl-Bt ± Amp ± Brt (ESM2, Fig. 3a-f, h, j-l). Replacement of Bt-Amp by secondary Chl (ESM2, Fig. 3k)	Sulfide content varies from < 5 vol.% sub- to anhedral disseminations and nodules (ESM2, Fig. 3b, e–f, j-k), mm-to-cm-scale laminae and stringers (ESM2, Fig. 3a, d, h), to up to m-scale semi-massive to massive lenses, commonly replacing fragmental volcanic units such as hyaloclastite in dacite (Fig. 5m; ESM2, Fig. 3g, i). Spongy and inclusion-rich textures (Fig. 5k-l; ESM2, Fig. 3j, l), with high-contrast BSE-imaging revealing micro-euhedral Py grains in the nodules (Fig. 5n). Overwhelmingly dominated by Po and Py. Sp-Ccp-Gn dominantly identified microscopically. All sulfides are strongly foliated and nodules filling relict amygdales are porphyroclastic with pressure shadows and the foliation wrapping around them (Fig. 5k; ESM2, Fig. 3g). Commonly with recrystallised and inclusion-poor rims (Fig. 5k; ESM2, Fig. 3j) or overgrown by secondary idiomorphic and inclusion-free Py	-8.21	+12.87	+2.01	≤0.52	-1.17	+3.42	-0.31	≤0.45
Po-Py-Mag ± Ccp ± Pn related to Qz-Cb-Grt-Amp-Px-Bt alteration (13)	Occur mainly in the southern part of the AWB, dominantly in felsic volcanic-volcaniclastic rocks of the MKD (ESM2, Fig. 4a-c, f) but is also observed in the HBB (Fig. 5o) and the AMKK (ESM2, Fig. 4e) Occur both as deformed with pre-kinematic textures (ESM2, Fig. 4a-e, m–n) and extensive recrystallisation to granoblastic textures (ESM2, Fig. 4j-l), as well as syn- to post-kinematic textures, overgrowing the foliation (ESM2, Fig. 4f-g). Occur as weak-intermediate patchy (ESM2, Fig. 4a-b) to m-scale intense and pervasive alteration (Fig. 5o; ESM2, Fig. 4c-f) in high-strain zones, parallel to slightly oblique to foliation and micro-folds (ESM2, Fig. 4f-g). Grt is dominated by Fe–Mn-Ca-Al endmembers (ESM2, Fig. 4g-j, l-n), and Amp and Px are dominated by Fe-rich endmembers (Fig. 5p-q; ESM2, Fig. 4i-l). Texture varies from decussate and granular (ESM2, Fig. 4h-i, q) to granoblastic (ESM2, Fig. 4j-l) and Grt-porphyroblastic (ESM2, Fig. 4m-n). Replacement by secondary Amp-Chl-Ep (ESM2, Fig. 4h-i)	Sulfide content varies from disseminations (Fig. 5p; ESM2, Fig. 4g-j, m) to mm-to-cm-scale semi-massive to massive bands and vein fill (Fig. 5q; ESM2, Fig. 4k, q). Pn mainly occur within or in the vicinity of ultramafic host rocks to the alteration (ESM2, Fig. 4p-q). Sulfides contain traces of Sp-Gn-Mol-Sch-CG-Apy-BiTe. Occur as anhedral, intergrown, granular masses in equilibrium with the alteration assemblage (Fig. 5p; ESM2, Fig. 4h-k, q), or as granoblastic, foliated, and folded lenses (Fig. 5o, q; ESM2, Fig. 4g, m), locally overprinted by the alteration assemblage and replaced by secondary Mag (ESM2, Fig. 4r)	-4.85	+12.93	-0.11	≤0.52	-1.5	-0.01	-0.72	≤0.45

Table 1 (continued)

Assemblage (number of samples)	Description	Sulfide content and textures	$\delta^{34}S$ (‰ V-CDT)				$\Delta^{33}S$ (‰)			
			Min	Max	Med	±2σ	Min	Max	Med	±2σ
Po-Pn ± Ccp in Srp and Tlc-Cb altered komatiite (24)	Vary from Srp-altered Ol-sulfide ± Chr adcumulate (Fig. 5r; ESM2, Fig. 5b) to Srp-altered orthocumulate with interstitial Tlc-Cb-Act-Tr (Fig. 5r; ESM2, Fig. 5c-d). Low-strain samples preserve magmatic cumulate texture with Srp pseudomorphs after sub- to euhedral Ol (Fig. 5r)	Occur as mm-to-cm-scale disseminated, irregular and interlobate blebs (Fig. 5r-s), cloudy blebs (ESM2, Fig. 5c-d), stringers (ESM2, Fig. 5f), or up to m-scale thick, massive accumulations (Fig. 5t) at the basal contact of the host komatiite. Vary from undeformed to highly strained. Intergrown with Mag (Fig. 5u). Sulfides and Chr are also partially re-placed by secondary Mag (ESM2, Fig. 5j-k)	-5.08	+2.94	-1.63	≤0.52	-1.11	+0.95	-0.53	≤0.45
VMS / BIF – literature* (12)			-11.3	+5.91	-0.12		-0.92	-0.36	-0.59	
Magmatic Ni sulfides – literature* (9)			-7.16	+0.53	+2.81		-0.69	-0.46	-0.53	

* Data from Bekker et al. (2009), C. Isaac (unpub. PhD thesis, 2015) and E. Lewis (unpub. BSc (Hons) thesis, 2019)

Ab albite, *Act* actinolite, *Alm* almandine, *AMKK* Agnew-Mount Keith Komatiite, *Amp* amphibole, *And* andalusite, *Apy* arsenopyrite, *AWB* Agnew-Wiluna Greenstone Belt, *Brt* barite, *BSE* backscatter electron, *Bt* biotite, *Cb* carbonate, *Ccp* chalcopyrite, *CD* Cosmos Dacite, *CG* cobaltite-gersdorffite, *Chl* chlorite, *Chr* chromite, *Cpx* clinopyroxene, *Crd* cordierite, *Cum* cummingtonite, *Ep* epidote, *Fsp* feldspar, *Gn* galena, *Gr* graphite, *Grt* garnet, *Gru* grunerite, *HBB* Hickies Bore Basalt, *Mag* magnetite, *MKD* Mount Keith Dacite, *Mol* molybdenite, *NCTB* Never Can Tell Basalt, *Ol* olivine, *Org* organic matter, *Pn* pentlandite, *Po* pyrrhotite, *Px* pyroxene, *Py* pyrite, *Qz* quartz, *Sch* scheelite, *Ser* sericite, *Sp* sphalerite, *Sps* spessartine, *Srp* serpentine, *BiTe* bismuth telluride, *Tlc* talc, *Tr* tremolite

Micro-euhedral and nodular pyrite with spongy textures and abundant gangue inclusions are widely recognised syn-sedimentary to early diagenetic sulfide textures (e.g., Rickard 2012; Steadman and Large 2016; Gregory et al. 2019). Similar spongy and nodular sulfide textures identified in metasedimentary rocks across the AWB (Fig. 5a-d; ESM2, Fig. 1j-m) therefore suggest a syn- to diagenetic timing of sulfide formation, i.e., prior to deformation and metamorphism. This is supported by deformed, pre-kinematic textures with the foliation wrapping around sulfide nodules (Fig. 5c) together with the common association of sulfides with organic material or graphite (ESM2, Fig. 1h), the latter of which may have aided sulfide precipitation (Rickard et al. 2007). The sulfide textures further reflect within-sediment growth, high degrees of fluid sulfide supersaturation, stagnant to gently advecting environments, and the supply of Fe and S enhanced over normal marine conditions, such as in fresh or brackish waters or from hydrothermal input (Rickard 2012; Gregory et al. 2019). Pyrrhotite with spongy and nodular textures is the dominant sulfide observed and interpreted to be diagenetic based on the textures (Fig. 5b-c). Pyrrhotite may also have formed as a replacement of diagenetic pyrite caused by desulfidation during medium- to high-grade metamorphism (e.g., Finch and Tomkins 2017). However, the transformation of pyrite to pyrrhotite would result in up to 30% volume reduction, extensive recrystallisation and formation of inclusion-poor or -free grains (e.g., Zhabin and Kremenetskiy 1993). As diagenetic textures appear to be preserved (Fig. 5b-d), we favour the diagenetic origin for spongy and nodular pyrrhotite. Steadman et al. (2015) reported similar diagenetic pyrrhotite from interflow sediments in the coeval volcanic sequences in the southern part of the Kalgoorlie Terrane, and suggested they may have formed under conditions with very low fO_2, high aH_2S, or high content of dissolved Fe^{2+}, such as in a closed basin environment. This may indicate that the AWB basin was to some extent closed off from the wider ocean prior to and during rifting, and thus prevented dilution with seawater. Sulfide contents, which locally exceed the few vol.% that are common in marine and lacustrine sediments (Rickard 2012), support minor hydrothermal input.

The generally positive $\Delta^{33}S$ signatures of the sulfides in the metasedimentary rocks are consistent with a dominantly reduced elemental S source (Fig. 6). The decreasing $\Delta^{33}S$ values approaching near zero is consistent with increasing mixing of the elemental S source with that of either dissolved sulfate-derived S with negative $\Delta^{33}S$, or S from magmatic-hydrothermal fluids with $\Delta^{33}S$ around zero (Fig. 6c). Such $\Delta^{33}S$ is compatible with a depositional environment being distal from the volcanic centre with only minor magmatic-hydrothermal fluid contribution to the S budget.

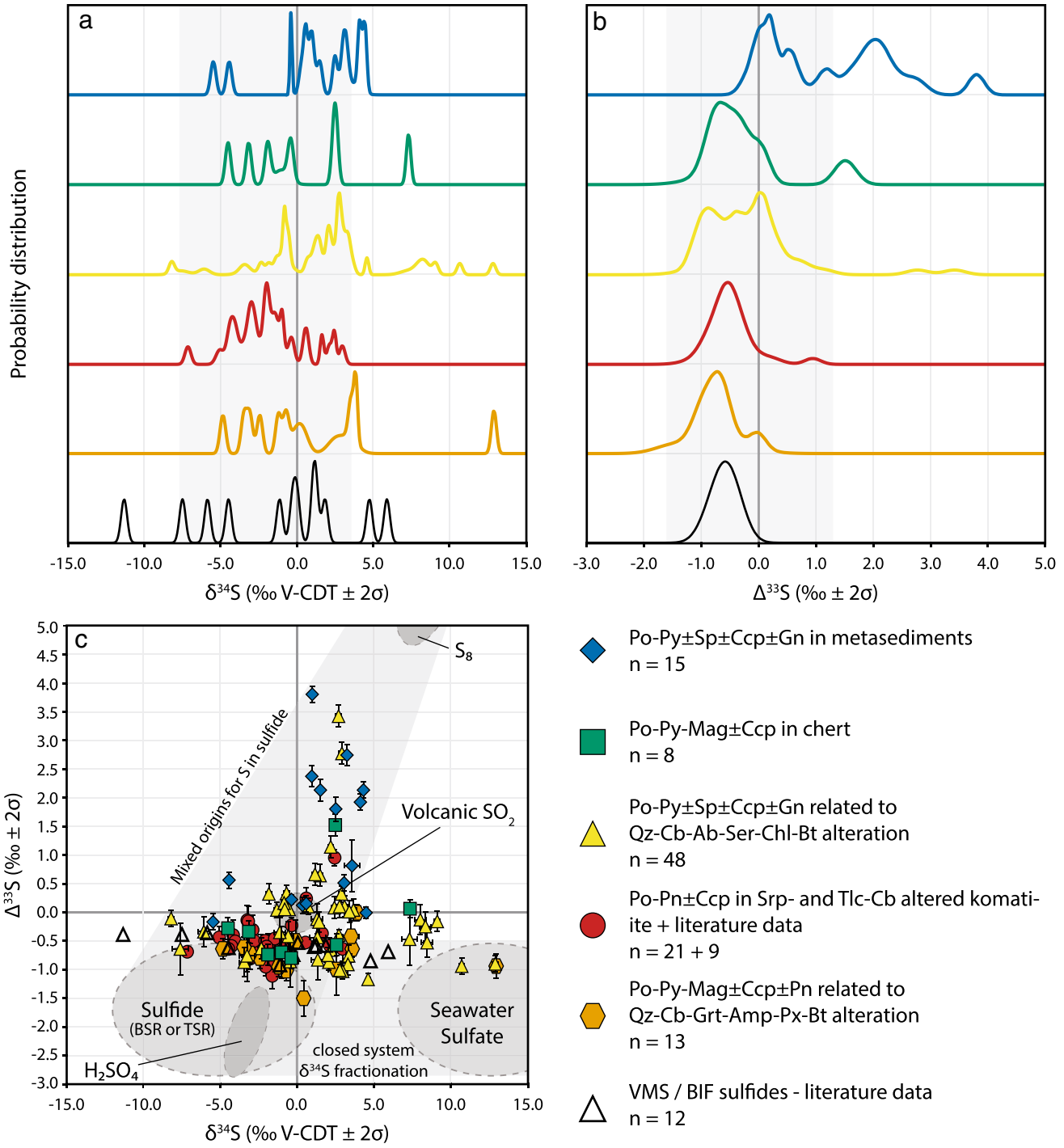

Fig. 6 Results of S-isotope analyses plotted with literature data from Bekker et al. (2009), C. Isaac (unpub. PhD thesis, 2015) and E. Lewis (unpub. BSc (Hons) thesis, 2019). **a**) and **b**) are probability distributions for $\delta^{34}S$ and $\Delta^{33}S$ for each sample group. The 2σ uncertainty for the literature data was assumed at ± 0.2‰. c) Plot of $\delta^{34}S$-$\Delta^{33}S$ for each of the sample groups with shaded areas representing the different S reservoirs from Fig. 1 (Ono et al. 2003). The $\delta^{34}S$ and $\Delta^{33}S$ values for each sample are presented as the average of their respective analyses, and the corresponding 2σ uncertainty is propagated for each sample average. Literature data is presented without their assumed uncertainties. Komatiite data from literature is combined with the pyrrhotite-pentlandite-chalcopyrite in serpentinised and talc-carbonate altered komatiite of this study. Abbreviations: Ab = albite, Amp = amphibole, BIF = banded iron formation, Bt = biotite, Cb = carbonate, Ccp = chalcopyrite, Chl = chlorite, Gn = galena, Grt = garnet, Mag = magnetite, Pn = pentlandite, Po = pyrrhotite, Px = pyroxene, Py = pyrite, Qz = quartz, Ser = sericite, Sp = sphalerite, Srp = serpentine, Tlc = talc, VMS = volcanogenic massive sulfides

Sulfidic BIF and vent-distal VMS sulfides

The mineralogy of the sulfidic chert and the interlayered sulfide-magnetite-bearing Fe–Mn-silicate laminae (Fig. 4i; Fig. 5e-f; ESM2, Fig. 2f-g) is consistent with high-grade metamorphism of a silicate-facies BIF (e.g., James 1954; Bekker et al. 2010). The deformed nature of the sulfidic chert and semi-massive to massive sulfide units (Fig. 4i; Fig. 5f), and the fact that they are folded with the rest of the Cycle 1–3 syn-rift stratigraphy, support our interpretation that these are syngenetic chemical sedimentary deposits. This is further supported by the granular, slightly spongy and inclusion-rich textures of the magnetite grains and nodules (Fig. 5g), which indicate a within-sediment diagenetic origin, as discussed in the sedimentary sulfide section above. Magnetite-sulfide mutual inclusions in the BIFs suggest a similar timing and precipitation environment for the sulfides (Fig. 5g). The gradual transition from sulfidic chert to metasiltstone and metashale indicates a similar deep, subaqueous environment for the formation of the sulfidic BIF. The common association with volcanic facies and transitional to sedimentary facies suggests that the BIFs are Algoma-type (Bekker et al. 2010), related to the transition from active volcanism to a period of volcanic quiescence and background sedimentation. In accordance with the interpretation from the sedimentary sulfides discussed above, Algoma-type BIF is noted to form in restricted basins, spatially related and transitional to VMS mineralisation (Huston and Logan 2004; Bekker et al. 2010). We therefore interpret the Fe-rich, but Cu–Zn-Pb poor semi-massive to massive sulfides transitional to the sulfidic BIFs as VMS mineralisation that formed slightly distal from the hydrothermal fluid vents (Galley et al. 2007).

A BIF and vent-distal VMS origin for the sulfides is supported by the dominantly negative $\delta^{34}S$ and $\Delta^{33}S$ values, consistent with derivation from thermochemical reduction of seawater sulfate (Fig. 6). A single $\Delta^{33}S$-positive sample indicates minor input from sedimentary sulfide, supporting the more vent-distal environment (Fig. 6b-c). The $\delta^{34}S$ values range from -4.5‰ to + 7.3‰ (Fig. 6a, c), which is consistent with either changing isotope composition of the fluid reservoir or with Rayleigh fractionation during sulfide precipitation (e.g., White 2018). The evidence from the sedimentary sulfides of enhanced supply of S in the AWB basin excludes Rayleigh fractionation as an explanation for the spread. Therefore, we interpret the range in $\delta^{34}S$ values to reflect the changes in the fluid reservoir. These changes were likely caused by varying degrees of mixing of hydrothermal fluids, which underwent varying degrees of SO_2 disproportionation during circulation in the crust, with either trapped porewater in sediments, or seawater upon venting.

Vent-proximal VMS sulfides

The pyrrhotite-pyrite ± sphalerite ± chalcopyrite ± galena sulfide assemblage with traces of barite (Fig. 5k-l, m; ESM2, Fig. 3l) is associated with the quartz-carbonate-albite-sericite-chlorite-biotite alteration assemblage in both mafic and felsic volcanic-volcaniclastic rocks (Fig. 5i-j; ESM2, Fig. 3c, k), indicating a syn-volcanic VMS-related origin (Galley et al. 2007). The pyrrhotite-pyrite dominated semi-massive to massive sulfides forming as replacements in fragmental volcanic facies (Fig. 5m) are, however, very poor in the common VMS minerals of sphalerite, chalcopyrite, and galena, which were only recognised microscopically (Fig. 5l, n). Remarkably similar barren VMS lenses replacing dacite hyaloclastite are locally found in the Nimbus VMS deposit in the southern part of the Kalgoorlie Terrane (Hollis et al. 2017), supporting a VMS interpretation for the massive sulfides and related alteration. The Nimbus deposit is currently the only known economic VMS deposit hosted in felsic and minor mafic volcanic-volcaniclastic rocks of a similar age as the Mount Keith Dacite and Never Can Tell Basalt in the AWB (Hollis et al. 2015, 2017). Multiple textural features further support the pre-kinematic nature of the sulfides, which precipitated prior to the onset of deformation and metamorphism (Vernon 2004). The most characteristic features include pressure shadows around sulfide grains (ESM2, Fig. 3j), lenses and nodules with the foliation deflecting around them (Fig. 5k; ESM2, Fig. 3j, m), as well as recrystallised, typically inclusion-poor idiomorphic metamorphic rims (Fig. 5k; ESM2, Fig. 3j, m). The occurrence of sulfides filling inter-pillow space in mafic rocks (Fig. 5j) and amygdales (Fig. 5k; ESM2, Fig. 3g) in both mafic and felsic rocks further indicates that the sulfides were introduced when space was open for fluid circulation. The spongy textures observed in the sulfide nodules with randomly oriented sulfide inclusions (Fig. 5k-l), especially the < 10 µm micro-euhedral pyrite identified in some of them (Fig. 5n), further support a syngenetic origin.

The S isotopic signatures of the pyrrhotite-pyrite ± sphalerite ± chalcopyrite ± galena sulfide assemblage are similar to but have a larger range than those of the BIF and vent-distal VMS sulfides with respect to both $\delta^{34}S$ and $\Delta^{33}S$ (Fig. 6). This spread may be due to a sampling bias between the two types but may also reflect the nature of the two reservoirs. The larger spread between negative, zero, and positive values of $\Delta^{33}S$ indicates a wider variety of both MIF and non-MIF S sources (Fig. 6b-c). This suggests more enhanced fluid circulation, leaching of pre-existing MIF-S heterogeneous crustal S, and fluid mixing, potentially with magmatic fluids, that is expected in more vent-proximal rather than vent-distal settings (Galley et al. 2007). We therefore propose that this sulfide assemblage is also part of a VMS system, forming the more vent-proximal part of a lateral continuum with the

sulfidic chert and BIF. As most of both sulfidic BIF and VMS mineralisation is found in the Never Can Tell Basalt and the Mount Keith Dacite, this highlights that hydrothermal fluid circulation due to heating and thinning of the crust was dominant during Cycle 3 in the AWB, consistent with the emplacement of the mantle upwelling and related thinning and heating of the crust. Most importantly, it means that the sedimentary and hydrothermal sulfides discussed above were all present in the stratigraphy at the time of komatiite eruption and may thus have contributed to the S source for the komatiites.

Sulfides associated with calc-silicate alteration

The quartz-carbonate-garnet-amphibole-pyroxene-biotite alteration assemblage (Fig. 5o; ESM2, Fig. 4) observed in felsic, mafic, and ultramafic lithologies occurs predominantly in the southern part of the belt. Two sub-types are recognised based on their textures: (i) pre-kinematic, highly deformed textures with the foliation wrapping around garnet porphyroblasts (ESM2, Fig. 4a-c), feldspar and quartz porphyroclasts in felsic lithologies (ESM2, Fig. 4a) and recrystallised amygdales in mafic lithologies. The Fe-Ca-Mn-Al-dominated mineralogy (Fig. 5p-q; ESM2, Fig. 4) is consistent with VMS or SEDEX related alteration metamorphosed at amphibolite- to granulite-facies conditions (e.g., Bonnet and Corriveau 2007; Theart et al. 2011; Dubé et al. 2014; Vikentyev et al. 2017); (ii) syn- to post-kinematic, with granular to decussate textures (ESM2, Fig. 4j-k, q) locally overprinting earlier foliation (ESM2, Fig. 4g). The mineralogy and textures are consistent with high-temperature skarn alteration related to granitic intrusions (e.g., Meinert et al. 2005), although similar skarn-like alteration has been recorded from contact metamorphosed VMS alteration, making it difficult to discern the origin for the syn- to post-kinematic calc-silicate assemblage (Vikentyev et al. 2017). Sulfides in the pre-kinematic assemblage were likely available for assimilation by the komatiite, however, this relationship is unclear for sulfides associated with the syn- to post-kinematic calc-silicate alteration. Nevertheless, as the Agnew-Mount Keith Komatiite is also overprinted by the syn- to post-kinematic calc-silicate alteration (ESM2, Fig. 4e, j), it clearly formed after emplacement of the komatiite in its current form. The timing is consistent with either contact metamorphism of previously formed VMS alteration or introduction of skarn alteration related to prolonged granitic plutonism during Cycle 4 and 5 basin inversion (Masurel et al. 2022).

Sulfides in skarn deposits commonly coincide with retrograde alteration, postdating the peak-skarn assemblages (Meinert et al. 2005). The sulfides associated with the syn- to post-kinematic calc-silicate alteration are both overprinted by and in textural equilibrium with the calc-silicate assemblage (Fig. 5p-q; ESM2, Fig. 4g-r), suggesting that at least some of the sulfides predated the alteration. The sulfides in textural equilibrium with the calc-silicate assemblage may have either been introduced by the skarn-forming fluids, remobilised from pre-existing crustal sulfides, or overprinted in-situ and subsequently metamorphosed and recrystallised together with the calc-silicate assemblage to form granoblastic textures (Vernon 2004). As the sulfide mineralogy of each sample generally mimics that of adjacent, un-altered rocks, such as the pentlandite-bearing sulfides in calc-silicate altered komatiite (ESM2, Fig. 4p), we favour the interpretation that the sulfides were pre-existing and simply overprinted by the calc-silicate alteration.

The overprint of pre-existing crustal and komatiite-hosted sulfides is supported by the sulfur isotope data: These overlap with the generally MIF-S negative BIF, VMS, and komatiite-hosted Ni-sulfides, but not with the generally MIF-S positive sedimentary sulfides (Fig. 6a-b) nor the granitic plutons surrounding the AWB, which have $\Delta^{33}S$ values ranging from approximately 0‰ to + 0.8‰ (Caruso et al. 2022). Granite-derived skarn forming fluids thus cannot account for the isotopic signatures in calc-silicate-hosted sulfides, highlighting the pre-existing nature of the latter. The fact that the syn- to post-kinematic calc-silicate alteration mainly overprinted hydrothermal crustal sulfides further indicates that the skarn-forming fluids were preferentially channelised along reactivated syn-rift faults, proximal to which the hydrothermal sulfides dominantly formed. This is consistent with reactivation of earlier growth faults during Cycle 4 and 5 granitic plutonism, uplift and basin inversion (e.g., Sibson 1995).

Komatiite-hosted magmatic sulfides and their preferred crustal S sources

The sulfides in the serpentinised and talc-carbonate altered komatiite samples (Fig. 4p-q; ESM2, Fig. 5) are generally unaltered and display primary magmatic blebby (Fig. 5r-s) to cloudy (ESM2, Fig. 5c-d) or massive textures (Fig. 5t), regardless of the alteration style. No apparent secondary sulfide overprinting has been observed (Fig. 5u). Therefore, the isotopic signatures of the sulfides could only have been modified by the later magnetite replacement during serpentinisation (Fig. 5u; ESM2, Fig. 5j). However, the magnetite-altered sulfides have overlapping S isotope signatures with unaltered sulfides, suggesting that serpentinisation did not alter the isotopic signatures of the sulfides. Similar preservation of S isotopic signatures has been observed in serpentinised komatiite at Black Swan (Caruso et al. 2020). We therefore suggest that the altered komatiites largely preserve their original magmatic sulfide assemblages and thus the S isotopic signatures of their crustal S sources, as recently established by Virnes et al. (2023).

The S isotope signatures of the magmatic Ni-sulfides predominantly overlap with those of the BIF and VMS sulfides (Fig. 6), consistent with previous observations by Bekker et al. (2009), which indicate that komatiites dominantly erupted upon or within hydrothermal sulfide-bearing strata, regardless of substrate lithology. As these sulfides mainly formed proximal to syn-rift faults, this highlights that proximity to the active rift and hydrothermal circulation may have been the dominant control on the formation of komatiite-hosted Ni deposit in the AWB.

Summary of sulfide facies relationships

The above interpreted sulfide facies associations reflect the lateral continuum between dominantly sedimentary environments through vent-distal, lower temperature hydrothermal environments towards higher temperature vent-proximal hydrothermal environments. This lateral variation also reflects the transition from seawater dominated fluids to magmatic-hydrothermal dominated fluids within the AWB rift basin. This variation is well illustrated in e.g., Bekker et al. (2009) and reproduced in Virnes et al. (2023) in the context related to this work. The following summary aims at framing the various sulfide facies into the AWB stratigraphic framework (Fig. 7; Masurel et al. 2022).

- Mantle upwelling, crustal melting, and the emplacement of the Cosmos Dacite on top of Youanmi-aged basement during Cycle 2 were characterised by the development of minor hydrothermal fluid convection cells and deposition of mainly lower temperature hydrothermal BIF and sedimentary sulfides in the Cosmos Dacite and underlying Youanmi crust, including the Hickies Bore Basalt (Fig. 7a).
- Cycle 2 was followed by the early Cycle 3 bimodal mafic-felsic volcanism and emplacement of the Never Can Tell Basalt and Mount Keith Dacite during the incipient rifting of the Youanmi crust (Fig. 7b).
- Incremental lithospheric thinning was assisted by the development of growth faults and magma flux, and led to the development of larger, more dynamic hydrothermal fluid convection cells. Related hydrothermal alteration and fluid venting caused the formation of VMS sulfides, especially along and near the extensional fault systems. Periods of volcanic quiescence promoted the deposition of lower temperature sulfidic BIF and chert, and distal sediments with associated sedimentary sulfides (Fig. 7c).
- During the subsequent emplacement of the Agnew-Mount Keith Komatiite, the komatiite flows thermomechanically eroded the upper crust proximal to syn-rift faults, which were areas of channelised fluid flow and more extensive hydrothermal alteration (Fig. 7d). This explains the observed preferential assimilation of vent-proximal VMS and lesser vent-distal BIF sulfides by the Agnew-Mount Keith Komatiite.
- The whole stratigraphic package was subsequently deformed and metamorphosed during Cycle 4 and 5 contemporaneously with granite plutonism and basin inversion. Rocks that formed proximal to reactivated syn-rift faults experienced high-temperature, granite-related skarn overprint (Fig. 7e).

Spatial relationship between S source reservoirs and komatiite-hosted mineralisation

The identification of different crustal S reservoirs, their link to the distinct stages of the evolving stratigraphy and the fact that the Agnew-Mount Keith Komatiite predominantly sourced VMS and lesser BIF sulfides enables a more holistic approach to understanding ore forming processes associated with komatiite magmatism. In the following section, we investigate the spatial variation of S isotope signatures of crustal and magmatic sulfides throughout the volcanic sequence of the central AWB (Cycle 2 and 3). This spatial analysis aims to elucidate the relationship(s) between the distribution of komatiite-hosted Ni-sulfides and their corresponding crustal S sources, which further enables us to evaluate the processes of transport, metal enrichment and deposition of assimilated crustal sulfides in komatiites.

Mount Keith region

In the Mount Keith region, we separated the magmatic Ni-sulfides in the Mount Keith Ultramafic unit and the underlying crustal sulfides (Fig. 8a) from those of the Cliffs Ultramafic unit and underlying crustal sulfides (Fig. 8b), as the structural attenuation in this region makes it difficult to distinguish the two systems. Similar to the findings of Bekker et al. (2009) and Fiorentini et al. (2012b), the magmatic Ni-sulfides in the Mount Keith Ultramafic unit in the Sarah's Find area (Fig. 8a, c) and the Mount Keith area (Fig. 8a, d) correlate well with the crustal sulfides in the underlying footwall rocks of the Mount Keith Dacite (Fig. 8c-d). This supports deposition of magmatic Ni-sulfides directly on top of, or within a few kilometres from their respective crustal S sources. Conversely, the crustal sulfides at Shed Well do not correlate well with the magmatic sulfides (Fig. 8a, e). This is likely due to a sampling bias and the small sample set, or to the fact that the magmatic Ni-sulfides were transported from a more distal source.

The $\Delta^{33}S$ values of the magmatic Ni-sulfides in the Cliffs Ultramafic unit show an excellent correlation with the crustal sulfides from the immediate footwall rocks, which are mostly the Never Can Tell Basalt (magmatic: -1.11‰ to + 0.24‰, median = -0.44‰; crustal: -1.17‰ to + 3.8‰, median = -0.12‰; Fig. 8b, f–h). There is a clear trend from

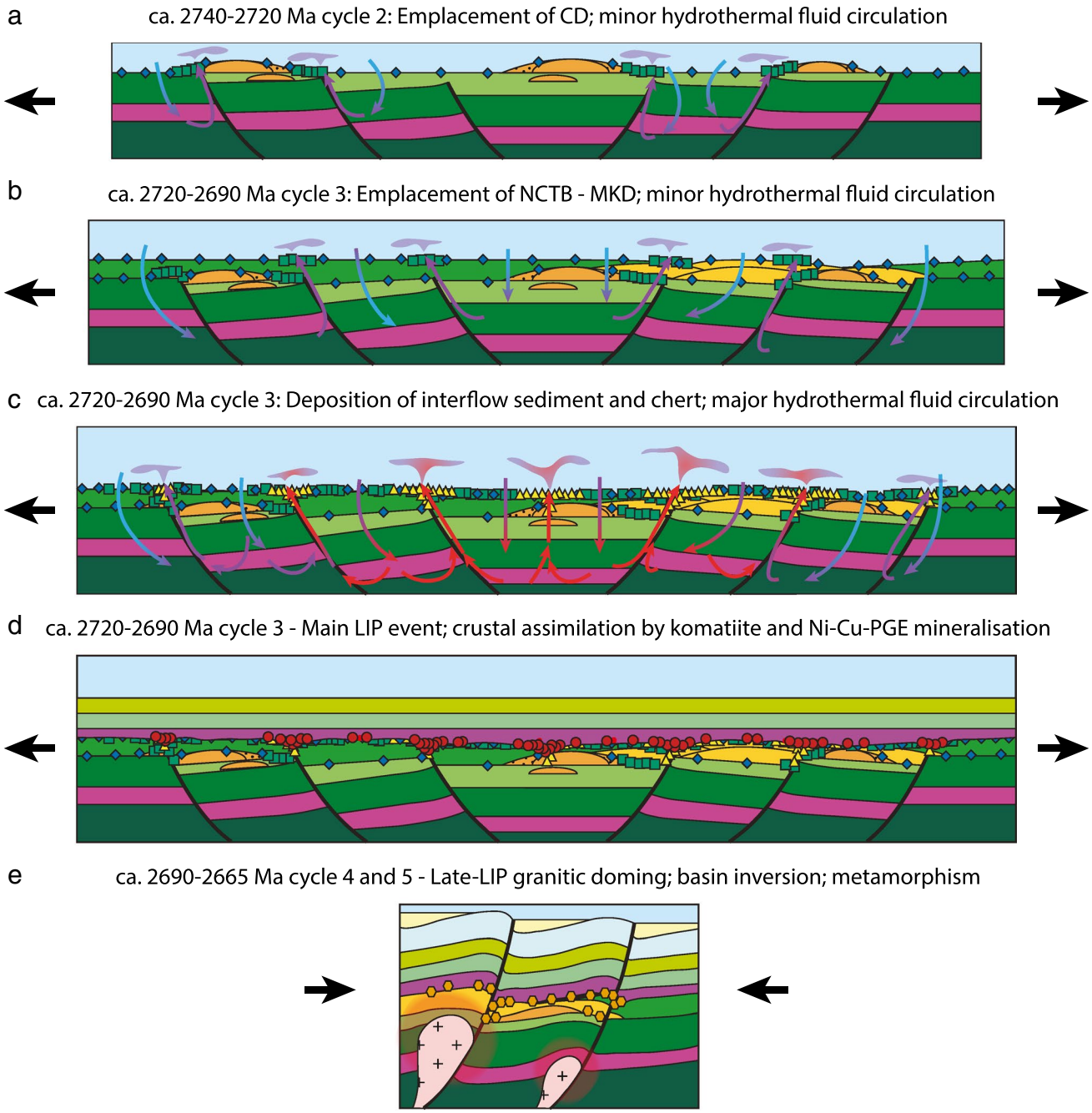

Fig. 7 Schematic sketch of the lateral variation of the crustal S sources in the evolving stratigraphy of the AWB within the Kalgoorlie-Kurnalpi intracratonic rift as interpreted by Masurel et al. (2022). The vertical scale of thinner stratigraphic units such as interflow sediments is exaggerated for the schematic purpose. Intrusive sills have been omitted and only one of the multiple interflow shale and chert layers are shown here for simplicity. Colours of the stratigraphic units follow those in Fig. 2b, and sulfide types follow those in Fig. 6. **a**) Cycle 2 emplacement of the Cosmos Dacite, minor hydrothermal convection cells and deposition of minor, lower temperature BIF-style hydrothermal sulfides and background sedimentary sulfides. **b**) Early Cycle 3 bimodal mafic-felsic volcanism and emplacement of the Never Can Tell Basalt and the Mount Keith Dacite along with continuous evolving of the hydrothermal convection cells and sulfide deposition. **c**) Volcanic paucity, deposition of interflow sediments and chert. Development of major hydrothermal convection cells due to the plume-induced heating of the crust. Consequent deposition of higher temperature VMS-style hydrothermal sulfides proximal to fluid vents, lower temperature BIF-style hydrothermal sulfides distal to fluid vents, along with background sedimentary sulfide deposition. **d**) Main LIP volcanism and emplacement of the Agnew-Mount Keith Komatiite. Thermomechanical erosion and assimilation of the crust by the komatiite and deposition of magmatic Ni-Cu-PGE sulfides in topographic lows. **e**) Cycle 4 Late-LIP felsic volcanism and granitic plutonism and Cycle 5 basin inversion and molasse deposition. Metamorphism of earlier formed alteration and related VMS, BIF, and sedimentary sulfides, potentially with minor granite-related calc-silicate overprint

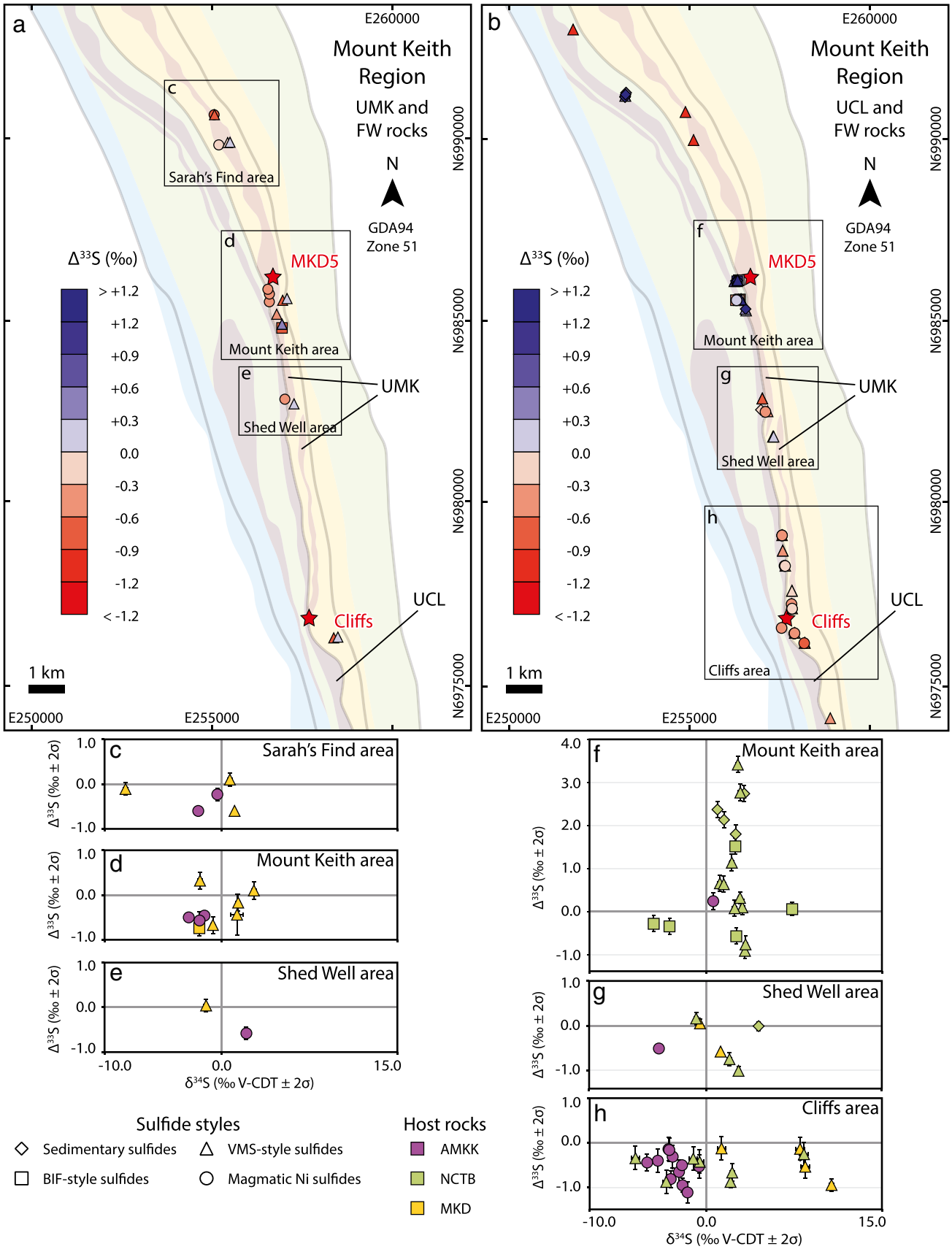
a
E260000
Mount Keith Region
UMK and FW rocks
N
GDA94 Zone 51
c
Sarah's Find area
d
MKD5
Mount Keith area
e
Shed Well area
UMK
UCL
Cliffs
Δ33S (‰)
> +1.2
+1.2
+0.9
+0.6
+0.3
0.0
-0.3
-0.6
-0.9
-1.2
< -1.2
1 km
N6990000
N6985000
N6980000
N6975000
E250000
E255000
b
E260000
Mount Keith Region
UCL and FW rocks
N
GDA94 Zone 51
f
MKD5
Mount Keith area
g
Shed Well area
UMK
h
Cliffs
Cliffs area
UCL
Δ33S (‰)
1 km
N6990000
N6985000
N6980000
N6975000
E250000
E255000
c
Sarah's Find area
d
Mount Keith area
e
Shed Well area
Δ33S (‰ ± 2σ)
1.0
0.0
-1.0
-10.0
0.0
15.0
δ34S (‰ V-CDT ± 2σ)
f
Mount Keith area
g
Shed Well area
h
Cliffs area
4.0
3.0
2.0
1.0
0.0
-1.0
Sulfide styles
Sedimentary sulfides
VMS-style sulfides
BIF-style sulfides
Magmatic Ni sulfides
Host rocks
AMKK
NCTB
MKD

◂**Fig. 8** Spatial distribution and S isotope variability of magmatic and crustal sulfides from the Mount Keith region. a) Distribution and $\Delta^{33}S$ signatures of magmatic sulfides from Mount Keith ultramafic unit and crustal sulfides from the underlying footwall rocks. b) Distribution and $\Delta^{33}S$ signatures of magmatic sulfides from the Cliffs Ultramafic unit and crustal sulfides from the underlying footwall rocks. c-h) $\delta^{34}S$-$\Delta^{33}S$ plots for each of the subareas (boxes in a and b) with sample colours based on the stratigraphic unit of the host rock. Samples without error bars in figures c-h are literature data. See Fig. 3 for lithology legend. Abbreviations: AMKK = Agnew-Mount Keith Komatiite; MKD = Mount Keith Dacite; NCTB = Never Can Tell Basalt; UCL = Cliffs Ultramafic unit; UMK = Mount Keith ultramafic unit

sedimentary dominated crustal sulfides in the Mount Keith area in the north (Fig. 8f), distal to the Cliffs Ni deposit, to hydrothermal dominated crustal sulfides in the south in the Cliffs area (Fig. 8h), proximal to the Cliffs Ni deposit. There is also an increasing variability in $\delta^{34}S$ of the crustal sulfides with proximity to the Cliffs Ni deposit ($\delta^{34}S_{max}$—$\delta^{34}S_{min}$ at Mount Keith area ~ 12‰ vs. $\delta^{34}S_{max}$—$\delta^{34}S_{min}$ at Cliffs area ~ 17‰; Fig. 8f-h). This north–south trend in the S isotope variability supports the interpretation that the Never Can Tell Basalt in the immediate footwall to the Cliffs Ni deposit represents the main locus for previous hydrothermal activity in this system. The increasing variability in $\delta^{34}S$ values towards this locus is likely caused by an intricate interplay between leaching of crustal sulfides by hydrothermal fluids, thermochemical sulfate reduction, fluid mixing near the zones of discharge or subsurface replacement, and fractionation between the different precipitating hydrothermal sulfides (e.g., Huston et al. 2023). It is inferred that crustal sulfides were then homogenised during assimilation by the Cliffs Ultramafic unit, but that the resulting magmatic Ni-sulfides from each area retained the mixed S isotopic signatures of the crustal sulfides in their respective immediate footwall rocks (Fig. 8f-h). This correlation suggests that the magmatic Ni-sulfides of the Cliffs Ultramafic unit were also deposited directly on top of or maximum within a few kilometres from their site of assimilation.

We cannot, however, rule out that some of the magmatic Ni-sulfides were transported by the Cliffs Ultramafic unit. At Shed Well, the $\Delta^{33}S$ value of the magmatic Ni–sulfide could have formed as a mix of the available hydrothermal crustal S sources in the immediate footwall rocks (Fig. 8g). However, the average $\delta^{34}S$ value of the magmatic sulfides is more negative than those of the crustal sulfides, an observation also noted by Fiorentini et al. (2012b). This suggests either that there is a sampling bias in our magmatic and/or crustal sulfide dataset, which failed to pick up the full range of S isotope signatures in that area, or that the magmatic Ni-sulfides were transported from the Mount Keith or Cliffs areas. Either way, the sample set is too small for this area to elaborate further. The key take-home message is that the data support our interpretation that both the MKD5 and Cliffs Ni deposits formed proximal to their respective crustal S sources, highlighting a new concept that mafic-hosted komatiites may be as prospective as felsic-hosted komatiites, contrary to previous interpretations (Fiorentini et al. 2012b).

Meredith Well region

The sample set in the Meredith Well region is limited (Fig. 9a-b). One sample of magmatic Ni-sulfides correlates well with being a mixture of both sedimentary and hydrothermal crustal sulfides from the proposed Cosmos Dacite unit, resulting in a $\Delta^{33}S$ value of ca. + 1.0‰ (Fig. 9b). The other two magmatic Ni–sulfide samples are more negative with respect to $\Delta^{33}S$ than any of the crustal sulfides (Fig. 9b). Given the small sample set we may simply have missed the full range of crustal sulfides present, with more MIF-S negative crustal sulfides to be found with further sampling and isotope analysis. Alternatively, the magmatic Ni-sulfides may have been transported from farther away. This inference is supported by the smaller $\delta^{34}S$ variation and larger $\Delta^{33}S$ variation, if the trend discussed above is indeed indicative of the crustal sulfide depositional environment as postulated here. However, the limited geochronological information available in the area prevents detailed stratigraphic correlations between this domain and other adjacent areas in the belt, including the Cosmos region (Fig. 3). More work is needed to establish a robust tectonostratigraphic framework for the Meredith Well area.

Perseverance region

In the Perseverance region, the $\Delta^{33}S$ values of the magmatic Ni-sulfides from the Perseverance Ultramafic Complex and 60A Ultramafic unit can be almost fully accounted for by the crustal sulfides available in the local footwall rocks (magmatic: -1.50‰ to -0.59‰, median = -0.64‰; crustal: -1.02‰ to + 0.81‰, median = -0.67‰; Fig. 10a-d). This further supports deposition of magmatic Ni-sulfides directly on top of or maximum within a few kilometres from their respective crustal S sources (Fig. 10c-d). However, some of the magmatic Ni-sulfides from the Perseverance-60A area (Fig. 10d) show more negative $\Delta^{33}S$ signatures than the crustal sulfides, indicating that the full S isotopic range of crustal sulfides has yet to be identified. It is possible that the source for these signatures were completely digested by the komatiite and thus not present in the stratigraphy anymore. The komatiite samples from the Camelot area did not yield any S isotope data, and thus cannot be compared with the crustal sulfides in this area (Fig. 10a-b).

The crustal sulfides in all areas of the Perseverance region are dominantly vent-proximal hydrothermal with negative $\Delta^{33}S$ signatures (Fig. 10a-d). Similar to sulfides in the Never Can Tell Basalt underlying the Cliffs Ultramafic unit in the

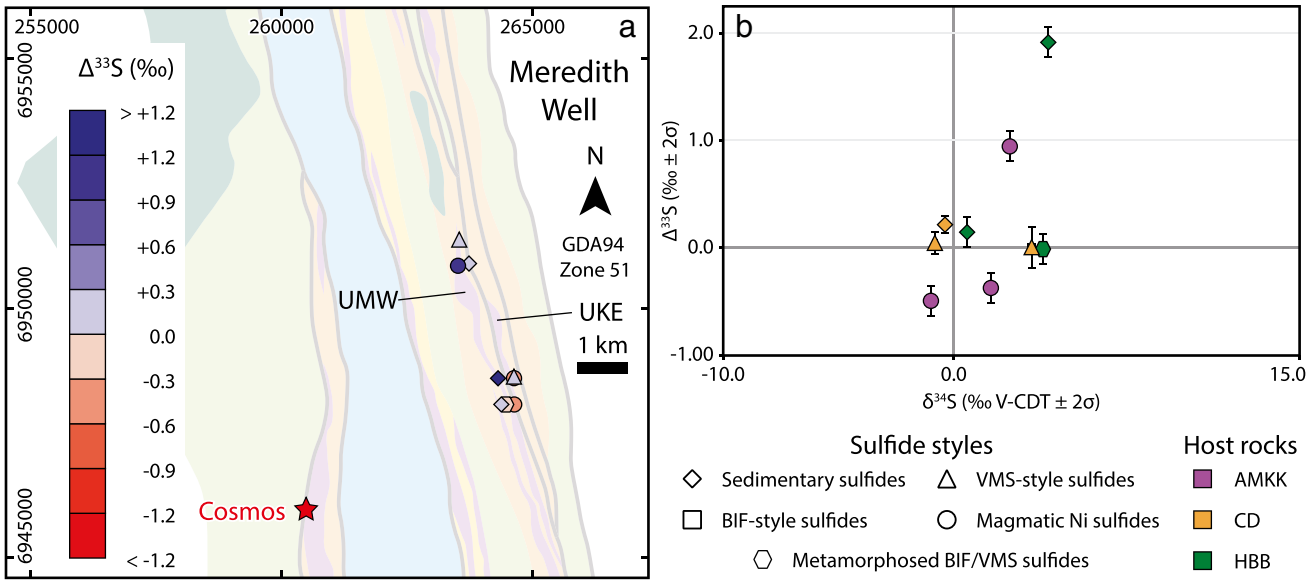

Fig. 9 Spatial distribution and S isotope variability of magmatic and crustal sulfides from the Meredith Well region. **a**) Distribution and $\Delta^{33}S$ signatures of magmatic sulfides from the Meredith Well Ultramafic unit and Kathleen East Ultramafic unit and crustal sulfides from the underlying footwall rocks. **b**) $\delta^{34}S$-$\Delta^{33}S$ plot of S isotope data for magmatic and crustal sulfides in the Meredith Well region with sample colours based on the stratigraphic unit of the host rock. See Fig. 3 for lithology legend. Abbreviations: AMKK = Agnew-Mount Keith Komatiite; CD = Cosmos Dacite; HBB = Hickies Bore Basalt; UKE = Kathleen East Ultramafic unit; UMW = Meredith Well Ultramafic unit

Mount Keith region (Fig. 8f-h) we see a north–south trend of increasing variability in $\delta^{34}S$ values ($\delta^{34}S_{max}$—$\delta^{34}S_{min}$ at Camelot area ~ 8‰, Fig. 10b; $\delta^{34}S_{max}$—$\delta^{34}S_{min}$ at Harmony area ~ 17‰, Fig. 10c; $\delta^{34}S_{max}$—$\delta^{34}S_{min}$ at Perseverance area ~ 21‰, Fig. 10d), which correlates with the decreasing presence of sedimentary and BIF sulfides (Fig. 10b-d). If the interpretation of the increasing variability in $\delta^{34}S$ values reflecting proximity to the locus of hydrothermal activity is true, then the Perseverance-60A area (Fig. 10a, d) would have been the most vent-proximal area in this region. Perhaps not surprisingly, the Perseverance Ni deposit (red star in Fig. 10a) is one of the largest komatiite-hosted Ni deposits in this region and in the world.

In summary, the mineralised komatiites in the Mount Keith (Fig. 8) and Perseverance regions (Fig. 10) appear to have dominantly assimilated vent-proximal VMS-style hydrothermal sulfides and deposited them proximal to their respective sites of assimilation. This is true for komatiites with both mafic and felsic volcanic and volcaniclastic stratigraphic substrates. The Meredith Well region (Fig. 9) is representative of a more vent-distal depositional environment and is not currently known to host significant Ni mineralisation. Importantly, there appears to be a general trend of large $\delta^{34}S$ variation with small $\Delta^{33}S$ variation of the crustal sulfides, indicative of a vent-proximal environment. Conversely, crustal sulfides with smaller $\delta^{34}S$ variation and larger $\Delta^{33}S$ variation may indicate a vent-distal to sedimentary environment. Where this trend is observed, the largest currently known Ni deposits, e.g., the Mount Keith MKD5, Cliffs, and Perseverance Ni deposits (Fig. 8; Fig. 10) correlate spatially with the most vent-proximal environment, regardless of stratigraphic footwall lithology.

Implications for sulfide transport and metal enrichment processes

It has been shown that metal exchange between silicate melts and sulfide liquids is largely driven by diffusion kinetics at the time scales of magmatic Ni–sulfide ore formation (Mungall 2002; Robertson et al. 2015a; Barnes and Robertson 2019). Consequently, metal enrichment of magmatic Ni-sulfides requires prolonged dynamic mixing and chemical equilibration with the komatiite silicate melt prior to settling and deposition to form economic concentration of magmatic Ni-sulfides. In laterally flowing komatiite systems, dynamic mixing can be simplified by considering two endmembers: lateral transport and density stratification of sulfide droplets in the turbulent komatiite flow, resulting in a basal massive sulfide deposit (Fig. 11a), or continuous settling and re-entrainment in dynamic traps such as the lee side of syn-rift faults, topographic lows and embayments, resulting in a disseminated sulfide deposit (Fig. 11b; Yao and Mungall 2021, 2022).

Nature is certainly more complex, and each komatiite-hosted Ni deposit may have formed from an intricate interplay between these two endmembers. However, if

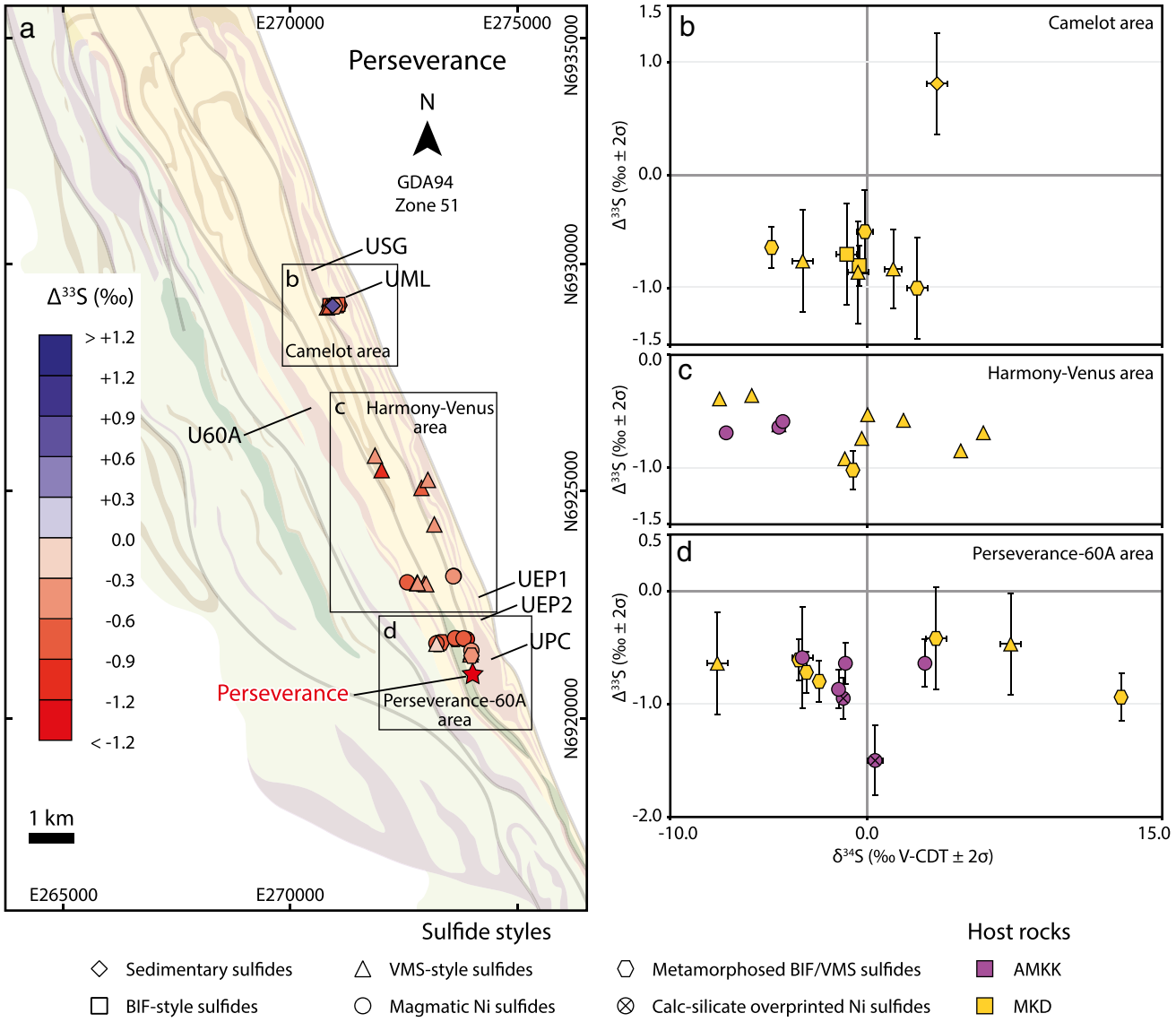

Fig. 10 Spatial distribution and S isotope variability of magmatic and crustal sulfides from the Perseverance region. **a**) Distribution and $\Delta^{33}S$ signatures of magmatic sulfides from the Perseverance Ultramafic Complex and 60A Ultramafic unit and crustal sulfides from the underlying footwall rocks. **b-d**) $\delta^{34}S$-$\Delta^{33}S$ plots for each of the sub-areas (boxes in a) with sample colours based on the stratigraphic unit of the host rock. Samples without error bars are literature data. See Fig. 3 for lithology legend. Abbreviations: AMKK = Agnew-Mount Keith Komatiite; MKD = Mount Keith Dacite; UEP1 = East Perseverance 1 Ultramafic unit, UEP2 = East Perseverance 2 Ultramafic unit, UML = Merlin Ultramafic unit, UPC = Perseverance Ultramafic Complex; USG = Sir Gawain Ultramafic unit, U60A = 60A Ultramafic unit

komatiite-hosted Ni deposits in the AWB predominantly formed proximal to their volcanic vents and sourced vent-proximal hydrothermal sulfide mineralisation from their stratigraphic substrates, then long lateral transport alone seems an unviable process of metal enrichment for the formation of economic accumulations of magmatic Ni-sulfides (Fig. 11a). Rather, re-circulation in dynamic traps such as syn-rift faults may have been the most dominant process for metal enrichment of the magmatic Ni-sulfides (Fig. 11b).

As discussed earlier, syn-rift faults also represent loci for enhanced hydrothermal fluid convection and sulfide deposition in VMS systems (e.g., Galley et al. 2007), which preceded the emplacement of komatiite flows. Areas proximal to these faults would have concentrated hydrothermal alteration and sulfide deposition regardless of whether the lithologies were mafic or felsic. The spread of the drill cores investigated in this study does not allow for estimating the extent or size of potential VMS lenses in substrate

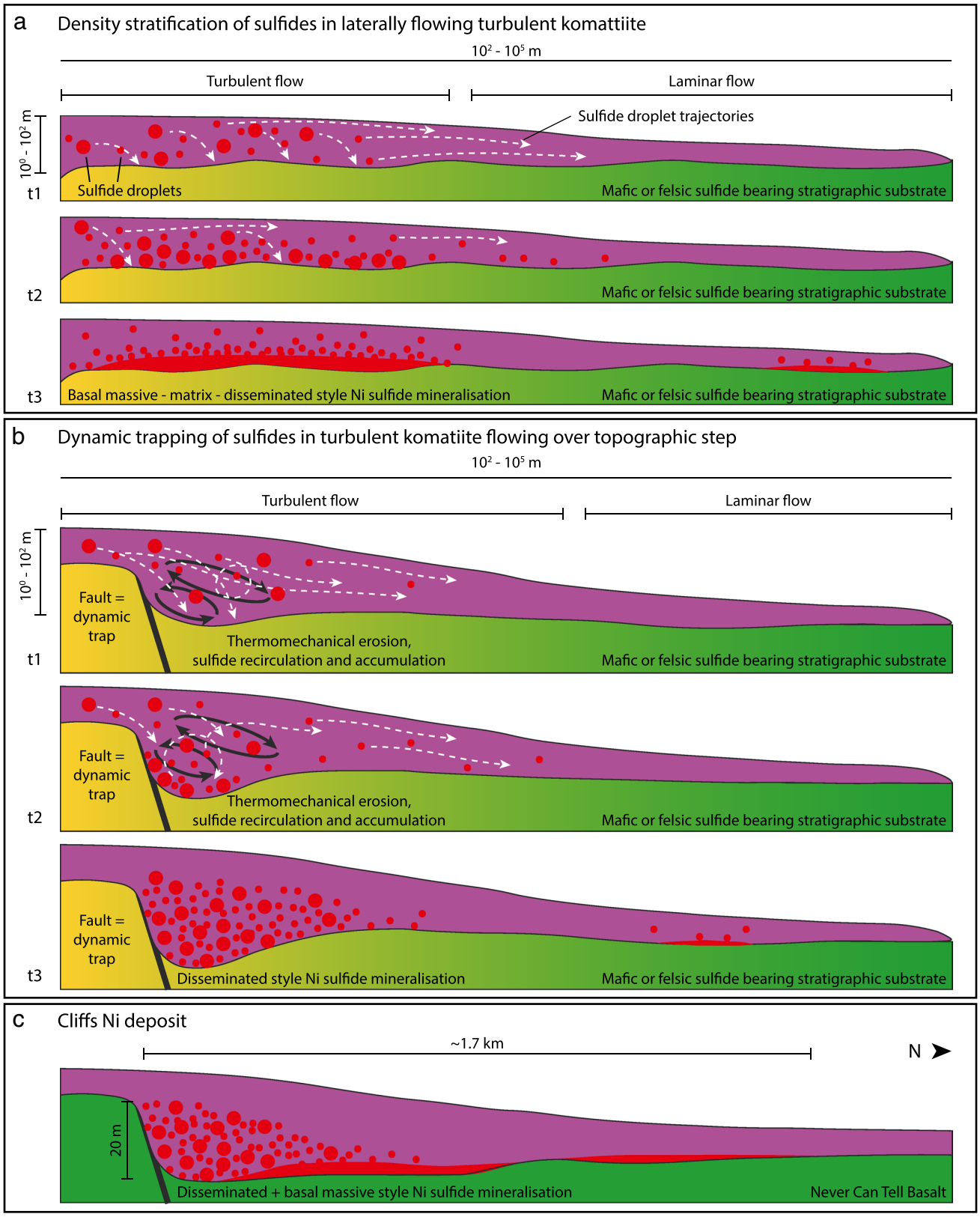
a
Density stratification of sulfides in laterally flowing turbulent komattiite
10² - 10⁵ m
Turbulent flow
Laminar flow
10⁰ - 10² m
Sulfide droplet trajectories
Sulfide droplets
t1
Mafic or felsic sulfide bearing stratigraphic substrate
t2
Mafic or felsic sulfide bearing stratigraphic substrate
t3
Basal massive - matrix - disseminated style Ni sulfide mineralisation
Mafic or felsic sulfide bearing stratigraphic substrate
b
Dynamic trapping of sulfides in turbulent komatiite flowing over topographic step
10² - 10⁵ m
Turbulent flow
Laminar flow
10⁰ - 10² m
Fault = dynamic trap
Thermomechanical erosion, sulfide recirculation and accumulation
t1
Mafic or felsic sulfide bearing stratigraphic substrate
Fault = dynamic trap
Thermomechanical erosion, sulfide recirculation and accumulation
t2
Mafic or felsic sulfide bearing stratigraphic substrate
Fault = dynamic trap
t3
Disseminated style Ni sulfide mineralisation
Mafic or felsic sulfide bearing stratigraphic substrate
c
Cliffs Ni deposit
~1.7 km
N
20 m
Disseminated + basal massive style Ni sulfide mineralisation
Never Can Tell Basalt

◂**Fig. 11** Endmembers of metal enrichment processes of crust-derived magmatic Ni-sulfides in komatiite flows, inspired by Yao and Mungall (2021, 2022). **a**) Sulfide density stratification during turbulent lateral flow and the formation of basal massive sulfide deposits. **b**) Dynamic trapping, sulfide recirculation and accumulation in the wake a topographic step, here represented by a syn-rift growth fault, resulting in a disseminated style sulfide deposit. **c**) Sketch of the Cliffs Ni deposit, interpreted to be a combination of initial dynamic trapping and formation of a disseminated style sulfide mineralisation, which was later remobilised to form basal massive sulfides < 2 km downstream from the fault. t = time

of the komatiites. However, the presence of locally > 10 m thick, deformed semi-massive to massive sulfides replacing dacite hyaloclastite indicates that such lenses were present prior to assimilation by the komatiites. The current extent of these may be smaller than originally due to assimilation by the komatiites. Considering the Perseverance Ni deposit with its ca. 1Mt of contained Ni (Mamuse et al. 2010), the total sulfide content would have to be ca. 6 Mt assuming a sulfide pentlandite content of 50%. Sizes of currently known VMS deposits globally range from 0.2 Mt to > 150 Mt of ore (Galley et al. 2007). A single large or several smaller VMS lenses would thus have provided an ample source of S for the komatiite. The weakened crust around the fault damage zones would have further enhanced the thermomechanical erosion by the komatiite as well as the dynamic trapping of the assimilated crustal sulfides. After metal upgrading in the dynamic traps the crust-derived magmatic Ni-sulfides may have been further transported downstream to be deposited e.g., where the komatiite transitioned from turbulent to laminar flow regime. This is exemplified by the Cliffs Ni deposit.

The Cliffs Ni deposit is a basal massive sulfide style deposit that formed at the base of the Cliffs Ultramafic unit. The prediction exemplified in the sketch of Fig. 11 therefore suggests that the Cliffs Ni deposit should have formed from lateral transport and density stratification rather than dynamic trapping. However, the S isotope data from this study together with 3D structural modelling by Perring (2015b) suggest that Cliffs indeed formed proximal to its S source and volcanic vent site. How is that compatible with the Ni mineralisation presumably having formed by lateral transport and sulfide density stratification? An examination of a long section of Cliffs Ni deposit (Fig. 12 in Perring 2015b) provides support for the apparent fact that basal massive Ni mineralisation at this deposit occurred via lateral transport and density stratification in a lava channel, the latter of which is highlighted by the Ni tenors of the massive sulfides. However, the massive sulfide lenses occur immediately downstream from a thicker zone of disseminated sulfides, which exists in the immediate wake of an interpreted syn-rift growth fault. We therefore propose that the Cliffs Ni deposit formed initially by dynamic trapping, recirculation, and accumulation of disseminated sulfides in the immediate wake of the growth fault topographic step. This was followed by remobilisation of the early forming disseminated sulfides downstream to form more massive basal sulfide accumulations < 2 km away from the growth fault (Fig. 11c). This process explains the similar crustal S source, the vent-proximal site of sulfide deposition and the similar tenors between the MKD5 and Cliffs Ni deposits, although the final mineralisation styles and the stratigraphic substrate lithologies are different. Ultimately, the new data and observations presented here highlight the importance of early crustal growth faults in the formation of komatiite-hosted Ni deposits rather than the lithology of the stratigraphic substrate to the mineralised komatiites.

Implications for process interpretation and exploration targeting: Revival of the $\delta^{34}S$

Due to the multitude of geological processes, which can cause mass-dependent fractionation of S isotopes, interpreting traditional $\delta^{34}S$ signatures applied to ore deposits and geological processes in general have historically been complicated (e.g., Lesher and Burnham 2001; Ripley and Li 2003). For magmatic Ni-deposits these signatures may often range within that of the mantle (e.g., Ripley and Li 2003) with post-magmatic metamorphic and/or hydrothermal modification invoked to explain excursions away from mantle values (Lesher and Keays 2002). Misleading mantle-like $\delta^{34}S$ signatures have been reported from e.g., the Bushveld Complex, were the corresponding non-zero $\Delta^{33}S$ values later revealed a crustal source for S for the Bushveld ores (e.g., Penniston-Dorland et al. 2008; 2012). Constraining $\delta^{34}S$ signatures to corresponding $\Delta^{33}S$ signatures can aid the identification of distinct sulfide facies that formed from different processes, thus preventing wrongful comparison. The $\Delta^{33}S$ signatures can further act as a control to enable proper utilisation of $\delta^{34}S$ signatures to inform on processes, which affected sulfides that formed from the same or similar sources. This utilisation is exemplified in e.g., the Wannaway Ni-deposit, where $\Delta^{33}S$-constrained $\delta^{34}S$ signatures were used to reveal the effects of S-degassing during komatiite emplacement (Caruso et al. 2017). Similar work at the Black Swan Ni-deposit revealed changes in $\delta^{34}S$ values during post-magmatic talc-carbonate alteration, while serpentinisation had little effect (Caruso et al. 2020). Our work has further shown that the textural and $\Delta^{33}S$-constrained sulfide facies can identify sulfides that formed from hydrothermal processes, whereafter their $\delta^{34}S$ variability can be a used to target the areas that experienced the most hydrothermal alteration. These areas are interpreted to coincide with syn-rift faults, where komatiites took advantage of the ample access to crustal S, weakened crust for enhanced

thermomechanical erosion, and increased topographical variation, the latter of which enhanced the process of metal enrichment of the magmatic Ni-sulfides through continuous recirculation (Yao and Mungall 2022).

Conclusions

In this study, we constrained the different crustal S reservoirs available for assimilation by bimodal mafic and felsic volcanic hosted komatiites during the ca. 2.7 Ga Kalgoorlie Large Igneous event in the AWB. We used multiple S isotopes to compare different crustal S reservoirs in mafic and felsic host rocks with komatiite-hosted Ni-sulfides to inform on the spatial distribution of the Ni deposits relative to their crustal S sources. We used this newly acquired knowledge to discuss the transport and metal enrichment processes of assimilated crustal sulfides in komatiite flows. The key outcomes of this work are:

- The crustal S reservoirs present prior to komatiite emplacement in the AWB comprise sedimentary to early diagenetic sulfides, vent-distal BIF-style exhalative or replacement style sulfides, and vent-proximal VMS-style exhalative or replacement sulfides;
- These sulfide styles represent lateral variation from rift-distal sedimentary sulfides to rift-proximal hydrothermal sulfides and are present in both mafic and felsic volcanic and sedimentary stratigraphic substrates to the komatiites;
- Komatiites with economic accumulations of Ni-sulfides predominantly assimilated vent-proximal VMS-style hydrothermal sulfides, regardless of their stratigraphic footwall lithologies;
- Komatiite-hosted Ni mineralisation was deposited proximal (< 5 km) to their respective crustal S sources;
- Metal upgrading of assimilated crustal sulfide droplets during transport in komatiite lava was promoted by multiple cycles of dynamic trapping and re-entrainment in the wake of topographic steps such as early growth faults;
- Early growth faults were the dominant loci for crustal weaknesses, hydrothermal alteration and the formation of exhalative or replacement VMS-style hydrothermal sulfides, which provided S for komatiites in more effective thermomechanical erosional sites;
- Proximity to the palaeo-rift centre and areas with evidence of earlier syn-volcanic seafloor hydrothermal fluid circulation appear to be the dominant control on the formation of Ni–sulfide mineralisation in komatiites;
- S isotopes applied to crustal S reservoirs may work as a proxy towards early growth faults and hydrothermal crustal sulfide accumulations, i.e., areas of higher komatiite-hosted Ni–sulfide prospectivity.

Supplementary Information The online version contains supplementary material available at https://doi.org/10.1007/s00126-024-01253-8.

Acknowledgements The authors would like to thank all the geology and technical staff at BHP Nickel West for facilitating the fieldwork, access to core yard and drillhole database, aiding the collection, cutting, and transportation of samples, invaluable discussions, and permission to publish this study. A special mention goes to Erin Western, Andrew Smith, Clayton Wright, Kyle Williams, and Dr. Clement Fay (BHP Nickel West) for fruitful discussions and providing datasets upon request. The authors acknowledge the facilities, and the scientific and technical assistance of Microscopy Australia at the Centre for Microscopy, Characterisation & Analysis, The University of Western Australia, a facility funded by the University, State and Commonwealth Governments. Dr. Laure Martin (Centre for Microscopy, Characterisation, and Analysis, CMCA, UWA) and Dr. Naomi Tucker (School of Earth Sciences, UWA) are thanked for their helpful discussions on petrography and interpretation of metamorphic and sulfide mineral textural relationships. Our gratitude goes to Dr. Zhuosen Yao and Dr. Jeffrey Steadman for their detailed and constructive comments, which greatly improved this manuscript.

Author contribution All authors contributed to the conceptualisation of this project. Fieldwork and sampling were conducted by Anne Brandt Virnes, Marco Fiorentini, Quentin Masurel, and Nicolas Thebaud. Sample preparation, petrography, SEM–EDS analysis, and statistical treatment of S isotope data were conducted by Anne Brandt Virnes. S isotope analysis by EA-IRMS and data reduction was conducted by Kim Baublys. All authors contributed to the data interpretation. Manuscript, figures, tables, and supplementary material were produced by Anne Brandt Virnes under the supervision of all other authors. The manuscript was extensively revised by Marco Fiorentini and Stefano Caruso, and revised and approved by all authors prior to submission.

Funding Open Access funding enabled and organized by CAUL and its Member Institutions. This project was conducted during the tenure of the University of Western Australia (UWA) Postgraduate Award for International Students and UWA International Fee Scholarship awarded to Anne Brandt Virnes. Field- and analytical work were funded by the Minerals Research Institute of Western Australia (MRIWA) M530 Yilgarn 2020 collaborative research project between the UWA, the Geological Survey of Western Australia (GSWA) and industry partners Northern Star Resources, Creasy Group, Gold Fields Limited, Gold Road Resources, Evolution Mining, and BHP Nickel West. BHP Nickel West further supported the project with in-kind contributions.

Declarations

Conflicts of interest The authors declare no competing or conflicts of interests relevant to this project.

References

Archibald NJ, Bettenay LF, Binns RA, Groves DI, Gunthorpe RJ (1978) The evolution of Archaean greenstone terrains, Eastern Goldfields Province, Western Australia. Precambrian Res 6:103–131. https://doi.org/10.1016/0301-9268(78)90008-6

Barnes SJ, Fiorentini ML (2012) Komatiite Magmas and Sulfide Nickel Deposits: A Comparison of Variably Endowed Archean Terranes. Econ Geol 107:755–780. https://doi.org/10.2113/econgeo.107.5.755

Barnes SJ, Robertson JC (2019) Time scales and length scales in magma flow pathways and the origin of magmatic Ni–Cu–PGE ore deposits. Geosci Front 10:77–87. https://doi.org/10.1016/j.gsf.2018.02.006

Barnes SJ, Hill RET, Gole MJ (1988) The Perseverance Ultramafic Complex, Western Australia: The Product of a Komatiite Lava River. J Petrol 29:305–331. https://doi.org/10.1093/petrology/29.2.305

Barnes SJ, Cruden AR, Arndt N, Saumur BM (2016) The mineral system approach applied to magmatic Ni–Cu–PGE sulphide deposits. Ore Geol Rev 76:296–316. https://doi.org/10.1016/j.oregeorev.2015.06.012

Baublys KA, Golding SD, Young E, Kamber BS (2004) Simultaneous determination of δ33SV-CDT and δ34SV-CDT using masses 48, 49 and 50 on a continuous flow isotope ratio mass spectrometer. Rapid Commun Mass Spectrom 18:2765–2769. https://doi.org/10.1002/rcm.1681

Bekker A, Barley ME, Fiorentini ML, Rouxel OJ, Rumble D, Beresford SW (2009) Atmospheric Sulfur in Archean Komatiite-Hosted Nickel Deposits. Science 326:1086–1089. https://doi.org/10.1126/science.1177742

Bekker A, Slack JF, Planavsky N, Krapež B, Hofmann A, Konhauser KO, Rouxel OJ (2010) Iron Formation: The Sedimentary Product of a Complex Interplay among Mantle, Tectonic, Oceanic, and Biospheric Processes. Econ Geol 105:467–508. https://doi.org/10.2113/gsecongeo.105.3.467

Beresford SW, Duuring P, Fiorentini ML, Rosengren NM, Bleeker W, Barley ME, Cas R, Tait M, Wallace H (2004) The structural and stratigraphic architecture of the Agnew-Wiluna Belt, Western Australia. AMIRA P710 Final Report, p 512

Bonnet A-L, Corriveau L (2007) Alteration vectors to metamorphosed hydrothermal systems in gneissic terranes In: Goodfellow WD (ed) Mineral deposits of Canada: A synthesis of major deposit-types, district metallogeny, the evolution of geological provinces, and exploration methods. Geol Assoc Canada, Miner Depos Div, Special Publ 5:1035–1049

Campbell IH, Griffiths RW, Hill RI (1989) Melting in an Archaean mantle plume: heads it's basalts, tails it's komatiites. Nature 339:697–699. https://doi.org/10.1038/339697a0

Canfield DE (2001) Biogeochemistry of Sulfur Isotopes. Rev Mineral Geochem 43:607–636. https://doi.org/10.2138/gsrmg.43.1.607

Caruso S, Fiorentini ML, Moroni M, Martin LAJ (2017) Evidence of magmatic degassing in Archean komatiites: Insights from the Wannaway nickel-sulfide deposit, Western Australia. Earth Planet Sci Lett 479:252–262. https://doi.org/10.1016/j.epsl.2017.09.035

Caruso S, Fiorentini ML, Barnes SJ, LaFlamme CK, Martin LAJ (2020) Microchemical and sulfur isotope constraints on the magmatic and hydrothermal evolution of the Black Swan Succession, Western Australia. Miner Deposita 55:535–553. https://doi.org/10.1007/s00126-019-00891-7

Caruso S, Fiorentini ML, Champion DC, Lu Y, Ueno Y, Smithies RH (2022) Sulfur isotope systematics of granitoids from the Yilgarn Craton sheds new light on the fluid reservoirs of Neoarchean orogenic gold deposits. Geochim Cosmochim Acta 326:199–213. https://doi.org/10.1016/j.gca.2022.03.023

Cassidy KF, Champion DC, Krapez B, Barley ME, Brown SJA, Blewett RS, Groenewald P, Tyler IM (2006) A revised geological framework for the Yilgarn Craton, Western Australia. Geological Survey of Western Australia Record, p 8

de Joux A (2014) Cosmos greenstone terrane: Insights into an Archaean volcanic arc, associated with komatiite-hosted nickel sulphide mineralisation, from U-Pb dating, volcanic stratigraphy and geochemistry. Unpub. PhD thesis. University of Edinburgh, p 271

de Joux A, Thordarson T, Denny M, Hinton RW, de Joux AJ (2013) U-Pb dating constraints on the felsic and intermediate volcanic sequence of the nickel-sulphide bearing Cosmos succession, Agnew-Wiluna greenstone belt, Yilgarn Craton. Western Australia. Precambrian Res 236:85–105. https://doi.org/10.1016/j.precamres.2013.06.008

de Joux A, Thordarson T, Fitton JG, Hastie AR (2014) The Cosmos greenstone succession, Agnew-Wiluna greenstone belt, Yilgarn Craton, Western Australia: Geochemistry of an enriched Neoarchaean volcanic arc succession. Lithos 205:148–167. https://doi.org/10.1016/j.lithos.2014.06.013

Ding T, Valkiers S, Kipphardt H, De Bièvre P, Taylor PDP, Gonfiantini R, Krouse R (2001) Calibrated sulfur isotope abundance ratios of three IAEA sulfur isotope reference materials and V-CDT with a reassessment of the atomic weight of sulfur. Geochim Cosmochim Acta 65:2433–2437. https://doi.org/10.1016/S0016-7037(01)00611-1

Dubé B, Mercier-Langevin P, Kjarsgaard I, Hannington M, Bécu V, Côté J, Moorhead J, Legault M, Bédard N (2014) The Bousquet 2-Dumagami World-Class Archean Au-Rich Volcanogenic Massive Sulfide Deposit, Abitibi, Quebec: Metamorphosed Submarine Advanced Argillic Alteration Footprint and Genesis. Econ Geol 109:121–166. https://doi.org/10.2113/econgeo.109.1.121

Farquhar J, Wing BA (2003) Multiple sulfur isotopes and the evolution of the atmosphere. Earth Planet Sci Lett 213:1–13. https://doi.org/10.1016/S0012-821X(03)00296-6

Farquhar J, Bao H, Thiemens M (2000) Atmospheric Influence of Earth's Earliest Sulfur Cycle. Science 289:756–758. https://doi.org/10.1126/science.289.5480.756

Farquhar J, Savarino J, Airieau S, Thiemens MH (2001) Observation of wavelength-sensitive mass-independent sulfur isotope effects during SO2 photolysis: Implications for the early atmosphere. J Geophys Res: Planets 106:32829–32839. https://doi.org/10.1029/2000JE001437

Farquhar J, Cliff J, Zerkle AL, Kamyshny A, Poulton SW, Claire M, Adams D, Harms B (2013) Pathways for Neoarchean pyrite formation constrained by mass-independent sulfur isotopes. PNAS 110:17638–17643. https://doi.org/10.1073/pnas.1218851110

Finch EG, Tomkins AG (2017) Pyrite-Pyrrhotite Stability in a Metamorphic Aureole: Implications for Orogenic Gold Genesis. Econ Geol 112:661–674. https://doi.org/10.2113/econgeo.112.3.661

Fiorentini ML, Barley ME, Pickard A, Beresford SW, Rosengren N, Cas R, Duuring P (2005) Age constraints of the structural and stratigraphic architecture of the Agnew-Wiluna greenstone belt: Implications for the age of komatiite-felsic association and interaction in the Eastern Goldfields Province, Western Australia. In: Minerals and Energy Research Institute of Western Australia, MERIWA Project M356, Report 255, p 39

Fiorentini ML, Beresford SW, Rosengren N, Barley ME, McCuaig TC (2010) Contrasting komatiite belts, associated Ni–Cu–(PGE) deposit styles and assimilation histories. Aust J Earth Sci 57:543–566. https://doi.org/10.1080/08120099.2010.492911

Fiorentini ML, Bekker A, Rouxel O, Wing BA, Maier WD, Rumble D (2012a) Multiple Sulfur and Iron Isotope Composition of Magmatic Ni-Cu-(PGE) Sulfide Mineralization from Eastern Botswana. Econ Geol 107:105–116. https://doi.org/10.2113/econgeo.107.1.105

Fiorentini ML, Beresford SW, Barley ME, Duuring P, Bekker A, Rosengren N, Cas R, Hronsky J (2012b) District to Camp Controls on the Genesis of Komatiite-Hosted Nickel Sulfide Deposits,

Agnew-Wiluna Greenstone Belt, Western Australia: Insights from the Multiple Sulfur Isotopes. Econ Geol 107:781–796. https://doi.org/10.2113/econgeo.107.5.781

Foster JG, Lambert DD, Frick LR, Maas R (1996) Re–Os isotopic evidence for genesis of Archaean nickel ores from uncontaminated komatiites. Nature 382:703–706. https://doi.org/10.1038/382703a0

Freda C, Baker DR, Scarlato P (2005) Sulfur diffusion in basaltic melts. Geochim Cosmochim Acta 69:5061–5069. https://doi.org/10.1016/j.gca.2005.02.002

Galley AG, Hannington MD, Jonasson I (2007) Volcanogenic massive sulphide deposits. In: Goodfellow WD (ed) Mineral deposits of Canada: a synthesis of major deposit-types, district metallogeny, the evolution of geological provinces, and exploration methods, vol Special Publ 5. Geological Association of Canada, Mineral Deposits Division, pp 141–161

Gole MJ, Barnes SJ, Hill RET (1987) The role of fluids in the metamorphism of komatiites, Agnew nickel deposit, western Australia. Contrib Mineral Petrol 96:151–162. https://doi.org/10.1007/BF00375229

Gole MJ, Western E, Diragitch A (2019) A revised stratigraphic model for the 2.7 Ga Agnew-Wiluna greenstone belt, Yilgarn Craton Western Australia. Ore Energy Resour Geol 1:100001. https://doi.org/10.1016/j.oreoa.2019.100001

Gregory D, Mukherjee I, Olson SL, Large RR, Danyushevsky LV, Stepanov AS, Avila JN, Cliff J, Ireland TR, Raiswell R, Olin PH, Maslennikov VV, Lyons TW (2019) The formation mechanisms of sedimentary pyrite nodules determined by trace element and sulfur isotope microanalysis. Geochim Cosmochim Acta 259:53–68. https://doi.org/10.1016/j.gca.2019.05.035

Hayman PC, Thébaud N, Pawley MJ, Barnes SJ, Cas RAF, Amelin Y, Sapkota J, Squire RJ, Campbell IH, Pegg I (2015) Evolution of a ~2.7Ga large igneous province: A volcanological, geochemical and geochronological study of the Agnew Greenstone Belt, and new regional correlations for the Kalgoorlie Terrane (Yilgarn Craton, Western Australia). Precambrian Res 270:334–368. https://doi.org/10.1016/j.precamres.2015.09.016

Herzig PM, Hannington MD (1995) Polymetallic massive sulfides at the modern seafloor a review. Ore Geol Rev 10:95–115. https://doi.org/10.1016/0169-1368(95)00009-7

Hill RET, Barnes SJ, Gole MJ, Dowling SE (1995) The volcanology of komatiites as deduced from field relationships in the Norseman-Wiluna greenstone belt, Western Australia. Lithos 34:159–188. https://doi.org/10.1016/0024-4937(95)90019-5

Hollis SP, Yeats CJ, Wyche S, Barnes SJ, Ivanic TJ, Belford SM, Davidson GJ, Roache AJ, Wingate MTD (2015) A review of volcanic-hosted massive sulfide (VHMS) mineralization in the Archaean Yilgarn Craton, Western Australia: Tectonic, stratigraphic and geochemical associations. Precambrian Res 260:113–135. https://doi.org/10.1016/j.precamres.2014.11.002

Hollis SP, Mole DR, Gillespie P, Barnes SJ, Tessalina S, Cas RAF, Hildrew C, Pumphrey A, Goodz MD, Caruso S, Yeats CJ, Verbeeten A, Belford SM, Wyche S, Martin LAJ (2017) 2.7Ga plume associated VHMS mineralization in the Eastern Goldfields Superterrane, Yilgarn Craton: Insights from the low temperature and shallow water, Ag-Zn-(Au) Nimbus deposit. Precambrian Res 291:119–142. https://doi.org/10.1016/j.precamres.2017.01.002

Huppert HE, Sparks RSJ, Turner JS, Arndt NT (1984) Emplacement and cooling of komatiite lavas. Nature 309:19–22. https://doi.org/10.1038/309019a0

Huston DL, Logan GA (2004) Barite, BIFs and bugs: evidence for the evolution of the Earth's early hydrosphere. Earth Planet Sci Lett 220:41–55. https://doi.org/10.1016/S0012-821X(04)00034-2

Huston DL, Laflamme C, Beaudoin G, Piercey S (2023) Light Stable Isotopes in Volcanic-Hosted Massive Sulfide Ore Systems. In: Huston D, Gutzmer J (eds) Isotopes in Economic Geology, Metallogenesis and Exploration. Springer International Publishing, Cham, Switzerland, pp 245–282

Isaac C (2015) Geochemistry of the north Eastern Goldfields, Western Australia: examining the processes that produce nickel sulphide camps. Unpub. PhD thesis. University of Western Australia, p 192

James HL (1954) Sedimentary facies of iron-formation. Econ Geol 49:235–293. https://doi.org/10.2113/gsecongeo.49.3.235

Kaye A, Thordarson T, Hayward C, Denny M, de Joux A (2010) The felsic and intermediate footwall to the Cosmos Nickel sulphide deposits, Agnew-Wiluna greenstone belt, Yilgarn Craton, Western Australia. In: SEG 2010 Conference proceedings: The challenge of finding new mineral resources: global metallogeny, innovative exploration, and new discoveries. Society of Economic Geologists, Keystone, p 5

Kent AJR, Hagemann SG (1996) Constraints on the timing of lode-gold mineralisation in the Wiluna greenstone belt, Yilgarn Craton, Western Australia. Aust J Earth Sci 43:573–588. https://doi.org/10.1080/08120099608728278

Konnunaho JP, Hanski EJ, Bekker A, Halkoaho TAA, Hiebert RS, Wing BA (2013) The Archean komatiite-hosted, PGE-bearing Ni–Cu sulfide deposit at Vaara, eastern Finland: evidence for assimilation of external sulfur and post-depositional desulfurization. Miner Deposita 48:967–989. https://doi.org/10.1007/s00126-013-0469-0

Lesher CM, Burnham OM (2001) Multicomponent elemental and isotopic mixing in Ni-Cu-(PGE) ores at Kambalda, Western Australia. Can Mineral 39:421–446. https://doi.org/10.2113/gscanmin.39.2.421

Lesher CM, Keays RR (2002) Komatiite-associated Ni-Cu-PGE deposits: Geology, mineralogy, geochemistry and genesis. In: Capri LJ (ed) The geology, geochemistry, mineralogy and Mineral beneficiation of the platinum-group elements, vol Special. Volume 54. Canadian Institute of Mining, Metallurgy and Petroleum, pp 579–617

Liu S, Hickman A, Langford R (1996) Stratigraphic correlations in the Wiluna greenstone belt. Western Aust Geol Surv Ann Rev 1994–1995:81–88

Lewis E (2019) Petrological and geochemical aspects of the 60A Ni sulphide mineralization, Western Australia. Unpub. B.Sc. (Hons) thesis. University of Queensland, p 128

Mamuse A, Beresford S, Porwal A, Kreuzer O (2010) Assessment of undiscovered nickel sulphide resources, Kalgoorlie Terrane, Western Australia: Part 1. Deposit and endowment density models. Ore Geol Rev 37:141–157. https://doi.org/10.1016/j.oregeorev.2010.02.004

Martin DM, Hocking RM, Riganti A, Tyler IM (2015) Geological map of Western Australia, 1:2 500 000 (14th edition), 14th edn. Geological Survey of Western Australia

Masurel Q, Thébaud N, Sapkota J, De Paoli MC, Drummond M, Smithies RH (2022) Stratigraphy of the Agnew-Wiluna Greenstone Belt: review, synopsis and implications for the late Mesoarchean to Neoarchean geological evolution of the Yilgarn Craton. Aust J Earth Sci 69:1149–1176. https://doi.org/10.1080/08120099.2022.2102076

Mavrogenes JA, O'Neill HSC (1999) The relative effects of pressure, temperature and oxygen fugacity on the solubility of sulfide in mafic magmas. Geochim Cosmochim Acta 63:1173–1180. https://doi.org/10.1016/S0016-7037(98)00289-0

McPhie J, Doyle M, Allen R (1993) Volcanic textures : a guide to the interpretation of textures in volcanic rocks. University of Tasmania, Hobart, Centre for Ore Deposit and Exploration Studies CODES

Meinert LD, Dipple GM, Nicolescu S (2005) World Skarn Deposits. In: Hedenquist JW, Thompson JFH, Goldfarb RJ, Richards JP (eds) Economic Geology; One Hundredth Anniversary Volume, 1905–2005. Society of Economic Geologists, Littleton, CO, pp 299–336

Mungall JE (2002) Kinetic Controls on the Partitioning of Trace Elements Between Silicate and Sulfide Liquids. J Petrol 43:749–768. https://doi.org/10.1093/petrology/43.5.749

Naldrett AJ, Turner AR (1977) The geology and petrogenesis of a greenstone belt and related nickel sulfide mineralization at

Yakabindie, Western Australia. Precambrian Res 5:43–103. https://doi.org/10.1016/0301-9268(77)90022-5
Nichols G (2009) Sedimentology and stratigraphy. Wiley-Blackwell
Ono S, Eigenbrode JL, Pavlov AA, Kharecha P, Rumble D, Kasting JF, Freeman KH (2003) New insights into Archean sulfur cycle from mass-independent sulfur isotope records from the Hamersley Basin, Australia. Earth Planet Sci Lett 213:15–30. https://doi.org/10.1016/S0012-821X(03)00295-4
Pawley MJ, Wingate MTD, Kirkland CL, Wyche S, Hall CE, Romano SS, Doublier MP (2012) Adding pieces to the puzzle: episodic crustal growth and a new terrane in the northeast Yilgarn Craton, Western Australia. Aust J Earth Sci 59:603–623. https://doi.org/10.1080/08120099.2012.696555
Penniston-Dorland SC, Wing BA, Nex PAM, Kinnaird JA, Farquhar J, Brown M, Sharman ER (2008) Multiple sulfur isotopes reveal a magmatic origin for the Platreef platinum group element deposit, Bushveld Complex, South Africa. Geology 36:979–982. https://doi.org/10.1130/g25098a.1
Penniston-Dorland SC, Mathez EA, Wing BA, Farquhar J, Kinnaird JA (2012) Multiple sulfur isotope evidence for surface-derived sulfur in the Bushveld Complex. Earth Planet Sci Lett 337–338:236–242. https://doi.org/10.1016/j.epsl.2012.05.013
Perring CS (2015a) A 3-D Geological and Structural Synthesis of the Leinster Area of the Agnew-Wiluna Belt, Yilgarn Craton, Western Australia, with Special Reference to the Volcanological Setting of Komatiite-Associated Nickel Sulfide Deposits. Econ Geol 110:469–503. https://doi.org/10.2113/econgeo.110.2.469
Perring CS (2015b) Volcanological and Structural Controls on Mineralization at the Mount Keith and Cliffs Komatiite-Associated Nickel Sulfide Deposits, Agnew-Wiluna Belt, Western Australia—Implications for Ore Genesis and Targeting. Econ Geol 110:1669–1695. https://doi.org/10.2113/econgeo.110.7.1669
Perring CS (2016) Yakabindie revisited—Volcanological and structural controls on the komatiite-hosted six mile well and Goliath North deposits and implications for the architecture of the 2.7 Ga rift event in the Agnew-Wiluna Belt, Yilgarn Craton. Western Australia. Econ Geol 111:1159–1185. https://doi.org/10.2113/econgeo.111.5.1159
Rickard D (2012) Sulfidic Sediments and Sedimentary Rocks. Elsevier
Rickard D, Grimes S, Butler I, Oldroyd A, Davies KL (2007) Botanical constraints on pyrite formation. Chem Geol 236:228–246. https://doi.org/10.1016/j.chemgeo.2006.09.011
Ripley EM, Li C (2003) Sulfur isotope exchange and metal enrichment in the formation of magmatic Cu-Ni-(PGE) deposits. Econ Geol 98:635–641. https://doi.org/10.2113/gsecongeo.98.3.635
Robertson JC, Barnes SJ, Le Vaillant M (2015a) Dynamics of Magmatic Sulphide Droplets during Transport in Silicate Melts and Implications for Magmatic Sulphide Ore Formation. J Petrol 56:2445–2472. https://doi.org/10.1093/petrology/egv078
Robertson JC, Ripley EM, Barnes SJ, Li C (2015b) Sulfur liberation from country rocks and incorporation in mafic magmas. Econ Geol 110:1111–1123. https://doi.org/10.2113/econgeo.110.4.1111
Rosengren NM, Beresford SW, Grguric BA, Cas RAF (2005) An intrusive origin for the komatiitic dunite-hosted Mount Keith disseminated nickel sulfide deposit, Western Australia. Econ Geol 100:149–156. https://doi.org/10.2113/100.1.0149
Rosengren NM, Cas RAF, Beresford SW, Palich BM (2008) Reconstruction of an extensive Archaean dacitic submarine volcanic complex associated with the komatiite-hosted Mt Keith nickel deposit, Agnew-Wiluna Greenstone Belt, Yilgarn Craton, Western Australia. Precambrian Res 161:34–52. https://doi.org/10.1016/j.precamres.2007.06.012
Sharman ER, Penniston-Dorland SC, Kinnaird JA, Nex PAM, Brown M, Wing BA (2013) Primary origin of marginal Ni-Cu-(PGE) mineralization in layered intrusions: Δ33S evidence from The Platreef, Bushveld, South Africa. Econ Geol 108:365–377. https://doi.org/10.2113/econgeo.108.2.365
Sibson RH (1995) Selective fault reactivation during basin inversion: potential for fluid redistribution through fault-valve action. Geological Society, London, Special Publications 88:3–19. https://doi.org/10.1144/gsl.Sp.1995.088.01.02
Steadman JA, Large RR (2016) Synsedimentary, Diagenetic, and Metamorphic Pyrite, Pyrrhotite, and Marcasite at the Homestake BIF-Hosted Gold Deposit, South Dakota, USA: Insights on Au-As Ore Genesis from Textural and LA-ICP-MS Trace Element Studies. Econ Geol 111:1731–1752. https://doi.org/10.2113/econgeo.111.7.1731
Steadman JA, Large RR, Meffre S, Olin PH, Danyushevsky LV, Gregory DD, Belousov I, Lounejeva E, Ireland TR, Holden P (2015) Synsedimentary to Early Diagenetic Gold in Black Shale-Hosted Pyrite Nodules at the Golden Mile Deposit, Kalgoorlie, Western Australia. Econ Geol 110:1157–1191. https://doi.org/10.2113/econgeo.110.5.1157
Szpak P, Metcalfe JZ, Macdonald RA (2017) Best practices for calibrating and reporting stable isotope measurements in archaeology. J Archaeol Sci: Reports 13:609–616. https://doi.org/10.1016/j.jasrep.2017.05.007
Theart HFJ, Ghavami-Riabi R, Mouri H, Gräser P (2011) Applying the box plot to the recognition of footwall alteration zones related to VMS deposits in a high-grade metamorphic terrain, South Africa, a lithogeochemical exploration application. Geochemistry 71:143–154. https://doi.org/10.1016/j.chemer.2010.09.002
Trofimovs J, Tait MA, Cas RAF, McArthur A, Beresford SW (2003) Can the role of thermal erosion in strongly deformed komatiite–Ni–Cu–(PGE) deposits be determined? Perseverance, Agnew-Wiluna Belt, Western Australia. Aust J Earth Sci 50:199–214. https://doi.org/10.1046/j.1440-0952.2003.00988.x
Vernon RH (2004) A practical guide to rock microstructure. Cambridge University Press, Cambridge
Vikentyev IV, Belogub EV, Novoselov KA, Moloshag VP (2017) Metamorphism of volcanogenic massive sulphide deposits in the Urals. Ore Geology. Ore Geol Rev 85:30–63. https://doi.org/10.1016/j.oregeorev.2016.10.032
Virnes AB, Fiorentini ML, Barnes SJ, Caruso S, Martin LAJ, Aleshin M, Schoneveld LE, Roberts MP, Masurel Q, Thebaud N (2023) Decoupling of sulfur isotope signatures from platinum group elements in komatiite-hosted ore systems: evidence from the Mount Keith MKD5 Ni-(Co-Cu) deposit. Western Australia. Econ Geol 118(8):1813–1834. https://doi.org/10.5382/econgeo.5030
Wanless VD, Perfit MR, Ridley WI, Klein E (2010) Dacite Petrogenesis on Mid-Ocean Ridges: Evidence for Oceanic Crustal Melting and Assimilation. J Petrol 51:2377–2410. https://doi.org/10.1093/petrology/egq056
White WM (2018) Stable Isotope Geochemistry. In: White WM (ed) Encyclopedia of Geochemistry: A Comprehensive Reference Source on the Chemistry of the Earth. Springer International Publishing, Cham, pp 1367–1374
Witt WK, Cassidy KF, Lu Y-J, Hagemann SG (2020) The tectonic setting and evolution of the 2.7 Ga Kalgoorlie-Kurnalpi Rift, a world-class Archean gold province. Miner Deposita 55:601–631. https://doi.org/10.1007/s00126-017-0778-9
Yao Z-s, Mungall JE (2021) Kinetic controls on the sulfide mineralization of komatiite-associated Ni-Cu-(PGE) deposits. Geochim Cosmochim Acta 305:185–211. https://doi.org/10.1016/j.gca.2021.05.009
Yao Z-S, Mungall JE (2022) Transport and deposition of immiscible sulfide liquid during lateral magma flow. Earth Sci Rev 227:103964. https://doi.org/10.1016/j.earscirev.2022.103964
Zhabin AG, Kremenetskiy AA (1993) The pyrite-pyrrhotite transformation as an ore-concentrating geochemical barrier. Int Geol Rev 35:359–368. https://doi.org/10.1080/00206819309465534